Generalized Diffusion Spectrum Magnetic Resonance Imaging (GDSI) for Model-free Reconstruction of the Ensemble Average Propagator

Qiyuan Tian[1,2,*], **Grant Yang**[1,2], **Christoph W.U. Leuze**[2], **Ariel Rokem**[3], **Brian L. Edlow**[4,5], **Jennifer A. McNab**[2]

[1]Department of Electrical Engineering, Stanford University, Stanford, California, United States

[2]Radiological Sciences Laboratory, Department of Radiology, Stanford University, Richard M. Lucas Center for Imaging, Stanford, California, United States

[3]eScience Institute, University of Washington, Seattle, Washington, United States

[4]Athinoula A. Martinos Center for Biomedical Imaging, Massachusetts General Hospital, Charlestown, Massachusetts, United States

[5]Center for Neurotechnology and Neurorecovery, Department of Neurology, Massachusetts General Hospital, Boston, Massachusetts, United States.

Abstract

Diffusion spectrum MRI (DSI) provides model-free estimation of the diffusion ensemble average propagator (EAP) and orientation distribution function (ODF) but requires the diffusion data to be acquired on a Cartesian q-space grid. Multi-shell diffusion acquisitions are more flexible and more commonly acquired but have, thus far, only been compatible with model-based analysis methods. Here, we propose a generalized DSI (GDSI) framework to recover the EAP from multishell diffusion MRI data. The proposed GDSI approach corrects for q-space sampling density non-uniformity using a fast geometrical approach. The EAP is directly calculated in a preferable coordinate system by multiplying the sampling density corrected q-space signals by a discrete Fourier transform matrix, without any need for gridding. The EAP is demonstrated as a way to map diffusion patterns in brain regions such as the thalamus, cortex and brainstem where the tissue microstructure is not as well characterized as in white matter. Scalar metrics such as the zero displacement probability and displacement distances at different fractions of the zero displacement probability were computed from the recovered EAP to characterize the diffusion pattern within each voxel. The probability averaged across directions at a specific displacement distance provides a diffusion property based image contrast that clearly differentiates tissue types. The displacement distance at the first zero crossing of the EAP averaged across directions orthogonal to the primary

[*]Correspondence to: Qiyuan Tian, Ph.D., Radiological Sciences Laboratory, Departments of Electrical Engineering and Radiology, Stanford University, Richard M. Lucas Center for Imaging, 1201 Welch Road, Stanford, California, USA, 94305. qytian@stanford.edu.

fiber orientation in the corpus callosum is found to be larger in the body (5.65±0.09 μm) than in the genu (5.55±0.15 μm) and splenium (5.4±0.15 μm) of the corpus callosum, which corresponds well to prior histological studies. The EAP also provides model-free representations of angular structure such as the diffusion ODF, which allows estimation and comparison of fiber orientations from both the model-free and model-based methods on the same multi-shell data. For the model-free methods, detection of crossing fibers is found to be strongly dependent on the maximum b-value and less sensitive compared to the model-based methods. In conclusion, our study provides a generalized DSI approach that allows flexible reconstruction of the diffusion EAP and ODF from multi-shell diffusion data and data acquired with other sampling patterns.

Keywords

Multi-shell acquisition; q-space imaging; diffusion spectrum imaging; ensemble average propagator; orientation distribution function; sampling density non-uniformity correction; model-free

Introduction

Q-space diffusion magnetic resonance imaging (QSI) provides model-free estimation of the diffusion ensemble average propagator (EAP, also known as spin displacement probability density function and diffusion spectrum) and diffusion orientation distribution function (ODF) only relying on a Fourier relationship between the attenuated echo signal in q-space and the EAP. In the 1960s, Stejskal and Tanner formulated the pulsed gradient spin echo (PGSE) nuclear magnetic resonance (NMR) experiment using the propagator language that Einstein used to formulate Fick's Law (1, 2). Stejskal and Tanner also proposed to recover the propagator of non-Gaussian diffusion and flow by taking a Fourier transform of signals measured by varying pulsed gradient direction and strength (3). To simplify the initial formalism, Kärger and Heink later introduced the concept of the EAP (4), which denotes the ensemble probability that spins at any starting position in a heterogeneous system displace by a certain displacement. In the 1980s, the PGSE NMR experiment was extended to MRI (5, 6). Callaghan then recast Stejskal and Tanner's formalism in terms of the wave vector, q (7), and proposed the concept of q-space, in analogy to k-space (8, 9). It was not until the mid-1990s that QSI was introduced to study the central nervous system (10, 11). In the early 2000s, Assaf and Cohen conducted a series of QSI studies (12) to infer the neuronal structure of bovine optic nerve (13, 14), rat brain (14) and spinal cord (15), and *in vivo* human brain (16, 17) from the EAP. Around the same time, Wedeen utilized QSI to delineate intra-voxel crossing fibers (known as diffusion spectrum imaging (DSI) (18-20)) for tracking white matter fiber pathways (i.e. tractography) in the *in vivo* human brain (21, 22) and proposed a new theory regarding the fundamental geometric structure of hemispheric fiber pathways (23). One limitation of DSI is that it only recovers the EAP and the diffusion ODF from q-space data acquired on a 3-dimension (3D) Cartesian grid. Here, we generalize the Cartesian DSI method by proposing a flexible framework that is also compatible with non-Cartesian (e.g. multi-shell) q-space data.

Even though the ODF is of great interest for tractography purposes, the EAP provides additional information of the tissue microstructure beyond fiber orientations. The EAP was found to be sensitive to the degree of myelination (24), and used to study spinal cord maturation (15) and degeneration (25) in the rat. In addition, the EAP may be used to characterize age-related white matter (WM) demyelination in healthy populations (26), differentiate lesions from normal appearing white matter and normal tissue in patients with multiple sclerosis (16, 17, 27), and detect remyelination within the multiple sclerosis lesions (24, 28). The EAP has also been used to map spinal cord diameter in an *ex vivo* rat (29, 30) and *in vivo* human axon diameters (31, 32). The various metrics derived from the EAP to characterize tissue microstructure properties include return-to-origin probability (or zero displacement probability) (12, 33-35), displacement distance at half maximum (12), kurtosis (24), mean-squared displacement (5, 12, 33), and fiber population dispersion (36), etc.

While model-based methods have several advantages, a model-free approach for recovering the EAP provided by DSI can be particularly valuable for studying brain regions where the tissue microstructure is not as well characterized as in white matter, such as in gray matter (GM), demyelinating lesion (16, 17, 24, 27, 28), hemorrhagic lesion (37, 38), or a tumor (39, 40). A model-free approach could also be valuable for diffusion measurements outside the brain (e.g. muscle (41-43)) or even potentially for studying vasculature (44).

Unfortunately, the use of DSI's Fourier relationship between the q-space signal and the EAP (Eq. 1) demands performing the Fast Fourier Transform (FFT) of q-space samples acquired on a 3D Cartesian grid (e.g. $11 \times 11 \times 11$ Cartesian grid with corners removed). The Cartesian sampling proposes several problems. Most importantly, the prescribed Cartesian q-space samples no longer locate on a strict Cartesian grid after the b-value and b-vector are corrected to account for gradient nonlinearity and subject motion (45-47), which decreases the accuracy of the FFT. Further, the Cartesian sampling is not optimal with many other analysis methods, such as diffusion tensor imaging (DTI) (48, 49), neurite orientation dispersion and density imaging (50) and the constrained spherical deconvolution (CSD) (51-53). In addition, the Cartesian diffusion data requires specialized data pre-processing. For example, the widely used "eddy" function (54) from the FMRIB Software Library (FSL) (55, 56) for eddy current correction and co-registration cannot process Cartesian data. The other problem with the Cartesian sampling is that the recovered EAP via the FFT also locates on a Cartesian grid, which is challenging to visualize and analyze (57). Last, the availability of Cartesian sampling protocols is limited on clinical MRI scanners.

Multi-shell q-space sampling has become the new standard for data acquisition. Some of the benefits of multi-shell sampling include the: (1) uniform angular resolution; (2) flexible sampling pattern and scan time (i.e. the number shells, and the b-value and the number of directions on each shell); (3) high compatibility with other processing and analysis methods; (4) capability to recover the EAP given sufficient sampling coverage, and (5) widely available protocols on clinical MRI scanners. Consequently, the multi-shell sampling scheme has been adopted by the MGH-USC (58-60) and WU-Minn-Ox (61-63) Human Connectome Project (HCP) to acquire gold standard diffusion data on a large population. Many widely used analysis methods which were originally proposed for single-shell diffusion data, such as q-ball imaging (QBI) (64-66), CSD and Bayesian estimation of

diffusion parameters obtained using sampling techniques for modeling crossing fibers (BEDPOSTX) (67), are now also compatible with multi-shell data.

Most EAP reconstruction methods using multi-shell data are based on DSI's Fourier relationship, but impose a q-space signal model, relinquishing the benefits that arise due to DSI being model-free. For example, the diffusion orientation transform (DOT) method (68, 69) assumes Gaussian diffusion. Alternatively, the multiple q-shell diffusion propagator imaging (mq-DPI) method (35, 70) models q-space signals as the solution of a Laplace equation in spherical coordinates. The Bessel Fourier orientation reconstruction (BFOR) (71) models q-space signals using the heat equation. The spherical polar Fourier imaging (SPFI) (72) method models q-space signals in terms of Gaussian-Laguerre polynomials. The mean apparent propagator (MAP)-MRI (73) method models q-space signals in terms of Hermite polynomials. For each approach, the accuracy and robustness to noise of the imposed model needs to be evaluated comprehensively for different microstructural configurations and q-space sampling schemes (e.g. maximum b-value).

Compared to the abundance of the model-based methods described above, there are very few model-free methods for reconstructing the EAP from multi-shell data. In hybrid diffusion imaging (HYDI), the multi-shell q-space samples are gridded to a Cartesian lattice (similar to k-space gridding (74)) for a FFT-based DSI reconstruction (75). The HYDI method has been used to directly compute EAP measures such as the zero displacement probability, mean-squared displacement and diffusion ODF but does not provide a complete solution of the EAP (33). The optimal way for gridding the q-space data has not been investigated. Further, the gridding process is also computationally expensive. Generalized q-sampling imaging (GQI) provides model-free diffusion ODF (76, 77) and has been applied to multi-shell radial q-space samples (78, 79). GQI, however, does not reconstruct the EAP.

In the current study, we developed a generalized DSI (GDSI) framework that is compatible with both Cartesian and non-Cartesian q-space diffusion MRI data. GDSI recovers the EAP in a preferable arbitrary coordinate system using the Discrete Fourier Transform (DFT). Scalar metrics such as zero displacement probability and displacement distance at half maximum can be easily computed from GDSI's EAP and are shown useful to characterize the diffusion process in different tissue types. Using GDSI's matrix formalism, the contribution and combination of q-space signals to the diffusion ODF is elucidated. The fiber crossing angles estimated by model-free and model-based methods are depicted. GDSI is tested on multiple different types of multishell datasets including those from the HCP.

Theory

In DSI, the EAP $P(\boldsymbol{r})$ is recovered from the Fourier transform of the normalized q-space signal $S(\boldsymbol{q})$ (7, 80-82) as:

$$P(\boldsymbol{r}) = \mathscr{F}(S(\boldsymbol{q})) = \int \int \int_{\boldsymbol{q} \in \mathbb{R}^3} S(\boldsymbol{q}) e^{-2\pi i \boldsymbol{q} \cdot \boldsymbol{r}} d\boldsymbol{q} \quad (1)$$

$\mathcal{F}$ denotes the Fourier transform, r is the 3D spatial vector describing a spin displacement ($r\boldsymbol{u}$, with $r=|r|$ the displacement distance and unit vector $\boldsymbol{u}$ the displacement direction), q is the gradient wave vector (or q-space points) describing the diffusion-encoding scheme ($q\boldsymbol{v}$, with $q=|\boldsymbol{q}|$ the encoding strength and unit vector $\boldsymbol{v}$ the encoding direction), q is proportional to the product of the strength and duration of a rectangle diffusion-encoding gradient, and proportional to the square root of b-value (Eq. A2).

As $S(q)$ is real and symmetric and $P(r)$ is real (41), the exponential function in Equation 1 can be reduced to a cosine function (76, 83) as:

$$P(\boldsymbol{r}) = \int \int \int_{\boldsymbol{q} \in \mathbb{R}^3} S(\boldsymbol{q})\cos(2\pi \boldsymbol{q} \cdot \boldsymbol{r})\, d\boldsymbol{q} \quad (2)$$

For a finite number (N) of measured q-space samples, the EAP is calculated as a linear weighted summation of all diffusion signals as:

$$P(\boldsymbol{r}) = \sum_{i=1}^{N} S(\boldsymbol{q}_i)\cos(2\pi \boldsymbol{q}_i \cdot \boldsymbol{r})\, \Delta \boldsymbol{q}_i \quad (3)$$

or in matrix form:

$$\underbrace{\begin{bmatrix} P(\boldsymbol{r}_1) \\ \vdots \\ P(\boldsymbol{r}_M) \end{bmatrix}}_{P} = \underbrace{\begin{bmatrix} \cos(2\pi \boldsymbol{q}_1 \cdot \boldsymbol{r}_1) & \cdots & \cos(2\pi \boldsymbol{q}_N \cdot \boldsymbol{r}_1) \\ \vdots & \ddots & \vdots \\ \cos(2\pi \boldsymbol{q}_1 \cdot \boldsymbol{r}_M) & \cdots & \cos(2\pi \boldsymbol{q}_N \cdot \boldsymbol{r}_M) \end{bmatrix}}_{F} \underbrace{\begin{bmatrix} \Delta \boldsymbol{q}_1 & & 0 \\ & \ddots & \\ 0 & & \Delta \boldsymbol{q}_N \end{bmatrix}}_{C} \underbrace{\begin{bmatrix} S(\boldsymbol{q}_1) \\ \vdots \\ S(\boldsymbol{q}_N) \end{bmatrix}}_{S} \quad (4)$$

P is a column vector ($M \times 1$) of recovered EAP values evaluated at spin displacements $r_j (1 \le j \le M, j \in \mathbb{Z})$. r_j can reside in an selected coordinate system, e.g. Cartesian or polar, to assistant the visualization and analysis of the EAP. F is the DFT matrix ($M \times N$). C is the diagonal q-space sampling density non-uniformity correction matrix ($N \times N$). S is a column vector ($N \times 1$) of the normalized attenuated echo signal measured at q-space location $q_i (1 \le i \le N, i \in \mathbb{Z})$.

Provided the gradient separation ( ) and duration (δ) are kept constant, the spin dephasing term ($\Phi = 2\pi qr$) in each element of matrix F can be expressed using the commonly reported b-value (b) and b-vector (v) of the diffusion pulse sequence following GQI's derivation (76) (see Appendix A):

$$F = \begin{bmatrix} \cos(\sqrt{6D_{water}b_1}\boldsymbol{v}_1 \cdot \lambda_1 \boldsymbol{u}_1) & \cdots & \cos(\sqrt{6D_{water}b_N}\boldsymbol{v}_N \cdot \lambda_1 \boldsymbol{u}_1) \\ \vdots & \ddots & \vdots \\ \cos(\sqrt{6D_{water}b_1}\boldsymbol{v}_1 \cdot \lambda_M \boldsymbol{u}_M) & \cdots & \cos(\sqrt{6D_{water}b_N}\boldsymbol{v}_N \cdot \lambda_M \boldsymbol{u}_M) \end{bmatrix} \quad (5)$$

D_{water} (2.5×10^{-3} mm^2/s) is the diffusion rate of free water at 37°C. $\lambda_j (1 \leq j \leq M, j \in \mathbb{Z})$ is the scalar that relates an arbitrary displacement distance r_j and the mean displacement distance of free water (MDD_{water}). $MDD_{water} = \sqrt{6D_{water}(\Delta - \delta/3)}$ is calculated using Einstein's equation (1) with effective diffusion time -δ/3 and an assumption of Gaussian diffusion. MDD_{water} is a constant number for all voxels, given the constant diffusion encoding timing and δ in a diffusion pulse sequence, and represents the longest displacement a spin can transverse in a specific experiment. It is more intuitive to express an arbitrary distance r_j as a ratio of this upper bound compared to using actual numbers.

Each diagonal element q_i of C represents the q-space volume associated with each q-space samples $q_i (1 \leq i \leq N, i \in \mathbb{Z})$. The signal measured at a sparsely sampled q-space location associates with a large q-space volume and is therefore scaled up, and vice versa.

To summarize the EAP's angular structure, the diffusion ODF is calculated by a radial integration of the EAP weighted by the displacement distance (r) to the power of n, along multiple directions as:

$$O_{r_s, r_e, n}(\boldsymbol{w}) = \int_{r_s}^{r_e} P(r\boldsymbol{w})r^n \, dr \quad (6)$$

Unit vector $\boldsymbol{w}$ denotes the direction along which the diffusion ODF is being computed. r_s and r_e is the starting and ending displacement distance along $\boldsymbol{w}$ respectively for the radial integration, n is the power of displacement distance. When n=0 (e.g. in QBI), the ODF represents the ensemble probability that spins displace along a certain direction. When n=2 (e.g. in DSI), the ODF represents the mean squared displacement distance along a certain direction. A larger n results in a diffusion ODF with higher contribution from the EAP at longer displacement distance.

The diffusion ODF can be calculated using a direct and indirect approach from the EAP. For the indirect approach, the EAP is first recovered along radial lines in the directions that the ODF will be reconstructed (using Eqs. 4 and 5) and then integrated. The EAP can be modified prior to ODF calculation, e.g. clipping the negative lobes of the ringing.

For the direct approach, the DFT and the radial integration are combined into a single step. The direct approach is advantageous for reducing computation and elucidating the relationship between q-space samples and the ODF, but does not allow modifying the EAP before the integration. Specifically, for a finite number of displacements with distances evenly spaced between r_s and r_e, ODF is calculated as a linear weighted summation of EAP values as:

$$O_{r_s, r_e, n}(\boldsymbol{w}) = \sum_{j=1}^{M} P(r_j\boldsymbol{w})r_j^n \Delta r_j (r_s \leq r_j \leq r_e) \quad (7)$$

or in matrix form:

$$
\underbrace{\begin{bmatrix} O_{r_s, r_e, n}(w_1) \\ \vdots \\ O_{r_s, r_e, n}(w_L) \end{bmatrix}}_{O_{r_s, r_e, n}} = \Delta r \underbrace{\begin{bmatrix} [r_1^n \cdots r_M^n] & \cdots & \mathbf{0} \\ \vdots & \ddots & \vdots \\ \mathbf{0} & \cdots & [r_1^n \cdots r_M^n] \end{bmatrix}}_{I_{r_s, r_e, n}} \underbrace{\begin{bmatrix} P(r_1 w_1) \\ \vdots \\ P(r_M w_1) \\ \vdots \\ P(r_1 w_L) \\ \vdots \\ P(r_M w_L) \end{bmatrix}}_{P} \tag{8}
$$

$O_{r_s, r_e, n}$ is a column vector ($L \times 1$) of recovered ODF values evaluated along directions w_k ($1 \le k \le L, k \in \mathbb{Z}$) for a given set of r_s, r_e and n. $r=(r_e - r_s)/(n-1)$ is a constant term accounting for the distance interval r_j for displacement r_j ($1 \le j \le M, j \in \mathbb{Z}$, $r_s \le r_j \le r_e$, $r_1 = r_s$, $r_M = r_e$). $I_{r_s, r_e, n}$ is the weighted summation matrix ($L \times ML$) of the radial integration of the EAP. P is a column vector ($ML \times 1$) of the EAP values along directions w_k at displacement distances r_j.

Substituting Equations 4 and 5 into 8 provides a solution for the ODF directly from the q-space signals:

$$\underbrace{\begin{bmatrix} O_{\lambda_s, \lambda_e, n}(\boldsymbol{w}_1) \\ \vdots \\ O_{\lambda_s, \lambda_e, n}(\boldsymbol{w}_L) \end{bmatrix}}_{O_{\lambda_s, \lambda_e, n}}$$

$$\Delta r \cdot$$

$$MDD_{water}^n \cdot \underbrace{\begin{bmatrix} \sum_{j=1}^M \cos(\sqrt{6D_{water}b_1}\boldsymbol{v}_1 \cdot \lambda_j\boldsymbol{w}_1) \cdot \lambda_j^n & \cdots & \sum_{j=1}^M \cos(\sqrt{6D_{water}b_N}\boldsymbol{v}_N \cdot \lambda_j\boldsymbol{w}_1) \cdot \lambda_j^n \\ \vdots & \ddots & \vdots \\ \sum_{j=1}^M \cos(\sqrt{6D_{water}b_1}\boldsymbol{v}_1 \cdot \lambda_j\boldsymbol{w}_L) \cdot \lambda_j^n & \cdots & \sum_{j=1}^M \cos(\sqrt{6D_{water}b_N}\boldsymbol{v}_N \cdot \lambda_j\boldsymbol{w}_L) \cdot \lambda_j^n \end{bmatrix}}_{R_{\lambda_s, \lambda_e, n}}$$

$$\underbrace{\begin{bmatrix} \Delta\boldsymbol{q}_1 & & 0 \\ & \ddots & \\ 0 & & \Delta\boldsymbol{q}_N \end{bmatrix}}_{C} \underbrace{\begin{bmatrix} S(\boldsymbol{q}_1) \\ \vdots \\ S(\boldsymbol{q}_N) \end{bmatrix}}_{S}$$

(9)

where λ_s λ_j λ_e (1 j M. ($j \in \mathbb{Z}$), $\lambda_j = \lambda_s = \lambda_s = r_s/MDD_{water}$. If r and MDD_{water}^n are set to 1, this only affects the scaling the absolute values of the ODF and therefore there is no loss of angular information. $R_{\lambda_s, \lambda_e, n}$ is the reconstruction matrix ($L \times N$) of ODF values. An ODF value $O_{\lambda_s, \lambda_e, n}(\boldsymbol{Wk})$ along a specific direction $\boldsymbol{w}_k$ is computed as a linear weighted summation of all sampling density corrected q-space signals, with linear weights determined by the kth row of $R_{\lambda_s, \lambda_e, n}(\boldsymbol{Wk})$.

Equation 9 formulates the DSI ODF reconstruction as a linear system, which provides an intuitive perspective to understand the relationship between the q-space signal and the ODF. To visualize the contribution and combination of q-space samples to the ODF, the row of $R_{\lambda_s, \lambda_e, n}$ for computing the ODF value along the q_z-axis (Fig. 1 bottom to top) was calculated, with parameters $\lambda_s=0$, $\lambda_e=1$, and n=0 ($R_{0,1,0}(qz)$ in Fig. 1a) or n=2 ($R_{0,1,2}(q_z)$ in Fig. 1b). $R_{0,1,0}(q_z)$ and $R_{0,1,2}(q_z)$ are displayed as 1D profile along the q_z-axis (Fig. 1a, c), 2D cross-section on the q_y-q_z plane (Fig. 1b, d), and 3D contour at single q(b)-values (Fig. 1e, f). The weights are rotationally symmetric about the q_z-axis (Fig. 1b, d, e, f), since the weight of a specific q-space sample is determined by the projection of its q-value to the q_z-

axis (i.e. $\sqrt{b_i}\mathbf{v}_i \cdot \mathbf{w}_k$ in Eq. 9). The 1D profile on the q_z-axis is a sinc function (76, 84) (Fig. 1a), or resembles the shape of a sinc function (Fig. 1c).

The 3D contours of $R_{0,1,0}(q_z)$ for high b-values (e.g. Fig. 1e, b ≥ 2000 s/mm^2) resemble thin discs (i.e., the weight for q-space points outside the q_x-q_y plane are close to zero), indicating that the ODF value along the q_z-axis is approximately the sum of signals on the equator of individual q(b)-values on the q_x-q_y plane, which is in agreement with QBI's use of the Funk-Radon transform. This approximation is more accurate (i.e. thinner disc) for higher b-values. In case of multiple q(b)-values, the ODF value along the q_z-axis can be approximated as the sum of signals on the entire q_x-q_y plane.

An ODF can be decomposed into component ODFs from individual q-space samples by rewriting Equation 9 as:

$$O_{\lambda_s, \lambda_e, n} = \Delta r \cdot R_{\lambda_s, \lambda_e, n} \cdot C \cdot \underbrace{\left(S(\mathbf{q}_1)\begin{bmatrix} 1 \\ 0 \\ \vdots \\ 0 \end{bmatrix} + S(\mathbf{q}_2)\begin{bmatrix} 0 \\ 1 \\ \vdots \\ 0 \end{bmatrix} + \cdots + S(\mathbf{q}_N)\begin{bmatrix} 0 \\ 0 \\ \vdots \\ 1 \end{bmatrix} \right)}_{S} = \sum_{i=1}^{N} S(\mathbf{q}_i) O_{\lambda_s, \lambda_e, n}^{\mathbf{q}_i}$$

(10)

$O_{\lambda_s, \lambda_e, n}^{\mathbf{q}_i}$ is the ith column of matrix $R_{\lambda_s, \lambda_e, n}$, representing the impulse response ODF from a unit signal q-space sample located at point $\mathbf{q}_i$. The impulse response ODF from q-space samples located on the q_z-axis with different q(b)-values are displayed in Figure 1e and 1f. $S(\mathbf{q}_i) O_{\lambda_s, \lambda_e, n}^{\mathbf{q}_i}$ is the component ODF from the q-space sample located at point $\mathbf{q}_i$.

Similarly, an ODF can also be decomposed into component ODFs from q-space samples with identical q(b)-values (i.e. individual shells).

Methods

Data Simulation

Simulations were performed with a multi-tensor model using the "multi_tensor" function of the Diffusion Imaging in Python (DIPY) software (13) (http://nipy.org/dipy/). Each individual tensor had an axial diffusion rate of 1.6×10^{-3} mm^2/s and a radial diffusion rate of 0.2×10^{-3} mm^2/s. A noise-free three-fiber-crossing voxel (Fig. 2) was simulated for illustration purpose, with each fiber contributing 55%, 25% and 20% of the total signal, using the standard DSI 11×11×11 Cartesian sampling (hereafter referred as DSI-11) with 7,000 s/mm^2 maximum b-value.

Data Acquisition

With Institutional Review Board (IRB) approval and written informed consent, data were acquired on a healthy subject using a clinical 3 Tesla MRI system (Discovery MR750, GE Healthcare, Milwaukee, Wisconsin) at Stanford. The scanner was equipped with a 32-channel radio frequency receive coil (Nova Medical, Wilmington, Massachusetts). A 2D single-refocused PGSE single-shot (SS) echo-planar-imaging (EPI) sequence was used to acquire multi-shell diffusion-weighted image (DWI) volumes of 30 contiguous axial slices covering the corpus callosum (CC). The data have: TE/TR=95.7/2000 ms, resolution=$2\times2\times2$ mm^3, diffusion time ( )=48.2 ms, gradient duration (δ)=31.8 ms, 6 shells (including q-space origin, hereafter referred to as MSL-6, $33\times$b=0, $103\times$b=1400 s/mm^2, $103\times$b=2800 s/mm^2, $103\times$b=4200 s/mm^2, $103\times$b=5600 s/mm^2, $103\times$b=7000 s/mm^2), ASSET parallel imaging factor R=2. Two non-DWI (b=0) volumes with reversed phase-encoding direction were acquired at the beginning of the scan. Non-DWI volumes were interleaved between every 16 DWI volumes.

Human Connectome Project Data

Pre-processed whole-brain T_1-weighted and multi-shell DW data of subject 1010 from the MGH-USC HCP consortium and subject 100307 from the WU-Minn-Ox HCP consortium were downloaded for analysis (https://www.humanconnectome.org/). The diffusion data from both sites were acquired using 2D single-refocused PGSE SS EPI sequences. The MGH-USC diffusion data have: resolution=$1.5\times1.5\times1.5$ mm^3, =21.8 ms, δ=12.9 ms, 5 shells (MSL-5, $40\times$b=0, $64\times$b=1000 s/mm^2, $64\times$b=3000 s/mm^2, $128\times$b=5000 s/mm^2, $256\times$10,000 s/mm^2), maximum q-value (q_{max})=0.12 μm^{-1} (85). The WU-Minn-Ox diffusion data have: resolution=$1.25\times1.25\times1.25$ mm^3, =43.1 ms, δ=10.6 ms, 4 shells (MSL-4, $18\times$b=0 s/mm^2, $90\times$b=1000 s/mm^2, $90\times$b=2000 s/mm^2, $90\times$b=3000 s/mm^2), q_{max}=0.0438 μm^{-1} (61). The MGH-USC T_1-weighted data were acquired with a multi-echo magnetization-prepared rapid acquisition gradient echo (ME-MPRAGE) sequence (86) at 1 mm isotropic resolution.

Image Processing

For the diffusion data acquired on-site at Stanford, the susceptibility-induced off-resonance field was estimated from the non-DWIs with opposite phase-encoding direction (87) using FSL's "topup" function. The susceptibility-induced EPI distortion, eddy current distortion, field drift and bulk motion were corrected simultaneously using FSL's "eddy" function. The two non-DWI volumes with reversed phase-encoding direction were not used within subsequent analysis steps.

Regions of Interest

For MGH-USC T_1-weighted data, cortical surface reconstruction and volumetric segmentation were performed using FreeSurfer software (88, 89) (https://surfer.nmr.mgh.harvard.edu/). The volumetric segmentation results (provided by aparc+aseg.mgz) were co-registered to the diffusion data using FreeSurfer's "bbregister" function with nearest neighbor interpolation. Binary masks of 14 regions of interest (ROIs) (i.e. ventricle, white matter (WM), CC, cerebellar WM, gray matter (GM), thalamus, accumbens,

amygdala, caudate, putamen, pallidum, hippocampus, brainstem, and cerebellar GM), each containing both hemispheres, were created. The ventricle mask was created using FreeSurfer's "mri_binarize" function with the "ventricles" option selected. The CC mask was created by combining masks of five sub-regions of CC, i.e. the anterior, mid-anterior, central, mid-posterior and posterior parts (Fig. 8g). Only voxels with FA from DTI larger than 0.5 in the CC mask were included. Three ROIs covering parts of pre- and post-central gyrus, through the center of the thalamus and the pons of the brainstem (red boxes in Fig.6 b-d) were manually selected on axial slices based on FreeSurfer's volumetric segmentation.

For the HCP data from both consortiums, binary masks of the WM were resampled from FreeSurfer's volumetric segmentation and eroded by one voxel.

For each dataset, one ROI located in the centrum semiovale (CSO) region (Fig. 10), containing the intersection of three white matter fiber bundles (the CC, the corona radiata (CR), and the superior longitudinal fasciculus (SLF)), was manually selected based on DTI FA maps. The ROIs from each dataset all contain 8×10 voxels, but cover slightly different spatial extension due to the different spatial resolution of each dataset. A voxel with intra-voxel crossing fibers from each dataset (Fig. 10 magenta dashed boxes) was selected for demonstration (Fig. 5, 9).

Q-space Sampling Density Correction

Numerical computation based on 3D Voronoi diagram (90) can be used for estimating the sampling density non-uniformity correction factor for various q-space sampling patterns. For multi-shell q-space samples, a simple geometry based approach was adopted (Fig. 4a), in a similar way that the correction factor is calculated for gridding the k-space data acquired with projection or radial trajectories (91).

Specifically, contours (middle shells) (Fig. 4a colored circles) were generated half-way between each q-space sampling shell to delineate the radial extent associated with each q-space sample. For the outermost q-space sampling shell, the outer radial extent (Fig. 4a bold green circle) was set to be an equal distance from the q-space sample as the inner contour boundary.

For the sample located at the q-space origin (a single sample for the averaged b=0 image), the correction factor is the volume of the central sphere. For DW samples located on each shell, the correction factor is the volume associated with the space between the inner and outer contours divided by the number of samples on the shell (assuming the q-space samples are uniformly distributed on each shell).

Mathematically, the correction factor V_{q_i} for a sample located on the ith shell with q-value q_i is:

$$V_{q_i} = \frac{\left(\frac{q_i + q_{i+1}}{2}\right)^3 - \left(\frac{q_i + q_{i-1}}{2}\right)^3}{N_{q_i} \cdot \left(\frac{q_2}{2}\right)^3} \quad (11)$$

where $q_0 = q_1 = 0$, $q_{ns+1} = (3q_{ns} - q_{ns-1})/2$, $q_i < q_{i+1}$, $1 \leq i \leq ns$. q_1 and q_2 correspond to the b=0 and smallest non-zero b-value. ns is the number of shells. N_{q_i} is the number of samples on a shell of q-value q_i.

The volume of the central sphere $\left(\frac{q_2}{2}\right)^3$ is divided such that the correction factor V_{q_1} for the q-space sample at origin is equal to 1 and therefore the normalized non-DW signal (equal to the sum of EAP values) is still 1 after density correction. As the diffusion time is kept constant, the q-value in Equation 11 can be replaced by the square root of the corresponding b-value (Eq. A3).

DSI and GDSI Reconstruction

The proposed GDSI (Eqs. 4, 5, 9) method was implemented in the framework of the DIPY software (available at https://github.com/qiyuantian/GDSI). For the simulated DSI-11 voxel, DSI reconstruction was performed using DIPY's "DiffusionSpectrumModel". The EAP was recovered on a Cartesian grid with a FOV of $2 \times MDD_{water}$ along each dimension. The diffusion ODF was computed by integrating the EAP (negative values clipped to 0) from the center to the MDD_{water}. GDSI reconstruction was performed with identical parameters as DSI reconstruction to obtain the EAP and diffusion ODF (i.e. $\lambda_s = 0$, $\lambda_e = 1$, n=2). Q-space sampling density correction was not used since q-space was uniformly sampled on a Cartesian grid. The GDSI ODF was computed using both the direct and indirect approach. For the direct approach, the impulse response ODF and the component ODF of each q-space sample were reconstructed. Component ODFs were computed for subsets of q-space signals with maximum b-values equal to: 0, 280 s/mm^2, 1120 s/mm^2, 2520 s/mm^2, 4480 s/mm^2, and 7000 s/mm^2. For the indirect approach, the negative values of the EAP were clipped to 0 (as performed in DSI) before calculating the ODF. The Pearson correlation of the EAP and ODF values from DSI and QSI reconstruction was reported.

For crossing-fiber voxels from the CSO region from each dataset, EAP was reconstructed with and without q-space sampling density correction, on a Cartesian grid with a FOV of $2 \times MDD_{water}$ along each dimension and along radial lines between 0 and MDD_{water}. The MDD_{water} for the Stanford, MGH-USC HCP and WU-Minn-Ox HCP data are 23.7 μm, 16.2 μm and 24.4 μm respectively.

For the MGH-USC HCP data, EAPs were recovered between 0 and MDD_{water} with q-space sampling density correction. Two scalar metrics were derived from the recovered EAPs:

(1) P_r: the probability at a specific displacement distance averaged across all EAP orientations;

(2) r_{α}: the displacement distance at which the probability density decays to a fraction α of the maximum probability (i.e. zero displacement probability P_0).

For the CC ROI, the displacement distance of the first zero crossing (r_0) was computed in the plane perpendicular to the primary eigenvector (V1) from DTI.

For each dataset, GDSI ODFs were reconstructed using the indirect approach with q-space sampling density and ringing removal (clipping the EAP values along each radial line beyond the first zero crossing to zero). The reconstruction parameters were λ_s=0, λ_e=0.8, n=2 for the Stanford and MGH-USC HCP data, and λ_s=0, λ_e=1, n=2 for the WU-Minn-Ox HCP data. The constant offset were removed. For voxels from the CSO ROI, the component ODFs from each single shell were also recovered.

The fiber orientations were delineated from the GDSI ODF using DIPY's "peaks_from_model" function. Specifically, the local maxima of a diffusion ODF with an amplitude larger than 5% of the global maximum were first detected. If the angle between the two directions of local maxima was less than 15 degrees, only the direction with the larger ODF amplitude was preserved. The directions were sorted according to their associated ODF amplitude. The first three directions were used as the primary, secondary and tertiary fiber orientations respectively.

DTI, BEDPOSTX, CSD and GQI Reconstruction

For each dataset, the DTI model was fitted using FSL's "dtifit" function using only those shells with b-values less than 1500 s/mm^2, to obtain the fractional anisotropy (FA) maps and V1.

The "ball and sticks" model was fitted using FSL's "bedpostx" function (3 sticks with a range of diffusivities). The estimated secondary and tertiary fiber orientations with fiber volume fraction lower than 5% were excluded.

Multi-shell multi-tissue CSD was performed using the MRTrix3 software (http://www.mrtrix.org/). The Stanford and MGH-USC HCP data were corrected for the B1 field inhomogeneity using MRTrix3's "dwibiascorrect" function. For each dataset, the segmentation of five tissue types (e.g. GM, WM) was first derived from the T_1-weighted data using MRTrix3's "5ttgen" function with the "fsl" option. The response functions were calibrated using MRTrix3's "dwi2response" function with the "msmt_5tt" option on brain voxels excluding the cerebellum. The fiber ODFs were then computed using MRTrix3's "dwi2fod" function. Three peaks for each fiber ODF were delineated using MRTrix3's "sh2peaks" function, without requirements on the peak amplitude. Within each voxel, the secondary and tertiary peaks were only preserved if their peak amplitudes were larger than 5% of the amplitude of the primary peak.

GQI reconstruction was performed using the "GeneralizedQSamplingModel" function from DIPY software. The reconstruction parameters were λ_s=0, λ_e=0.8, n=2 for the Stanford and MGH-USC HCP data, and λ_s=0, λ_e=1, n=2 for the WU-Minn-Ox HCP data, same as those used in GDSI. The fiber orientations were delineated from the GQI ODF using DIPY's "peaks_from_model" function in the same way as that used in GDSI.

Statistical Analysis

For the MGH-USC HCP data, the mean and standard deviation of P_r and r_a within the 14 FreeSurfer ROIs were reported. The Pearson correlation of the T_1-weighted and P_0 values of brain voxels was reported. The mean and standard deviation of r_0 perpendicular to DTI V1 within the five FreeSurfer CC sub-regions were reported.

For the HCP data, the crossing angle in WM voxels between the primary and secondary fibers, the primary and tertiary fibers, and the secondary and tertiary fibers estimated using BEDPOSTX, CSD and GDSI were computed. The angle between two directions (**v1**, **v2**) was computed as $\cos^{-1}(|\mathbf{v1 \cdot v2}|)$, ranging between ([0, 90°]).

Results

Our proposed DFT-based GDSI is equivalent to FFT-based DSI reconstruction. The EAPs (Fig. 2a, b) and diffusion ODFs (Fig. 2d-f) recovered from the simulated DSI-11 voxel using the two methods are qualitatively similar and quantitatively highly correlated (correlation larger than 0.995). The amplitudes along some directions on GDSI ODF (Fig. 2d, e, g pink arrows) computed using the direct approach are lower than those on DSI ODF, because the negative EAP values were not clipped to 0 in the direct approach.

GDSI's linear system formalism of the diffusion ODF reconstruction elucidates the contribution of q-space signals to a diffusion ODF. The diffusion ODF (reconstructed using the direct approach) from the simulated DSI-11 voxel (Fig. 3d) is a summation of 515 component ODFs (Fig. 3c, $S(\boldsymbol{q}_i)O_{\lambda_s,\lambda_e,n}^{\boldsymbol{q}_i}$ in Eq. 10). Each component ODF is a multiplication of the signal intensity (Fig. 3a, arranged from low to high q(b)-value, in the left to right, top to bottom order) and the corresponding impulse response ODF (Fig. 3b, a column of $R_{\lambda_s,\lambda_e,n}$ in Eq. 9) at a specific q-space sampling location. As the q(b)-value increases, the angular variation (high frequency information) of the impulse response ODF and component ODF increases, while the contribution (size) of the component ODFs to the combined ODF decreases. The combined diffusion ODF becomes sharper as more signals from high q(b)-values are included (Fig. 3e). Notably, the impulse response ODF and component ODF have both positive and negative values, while their summation is guaranteed to produce non-negative diffusion ODF.

Figure 4b displays the estimated q-space sampling density non-uniformity correction factors at each shell for the Stanford, MGH-USC HCP and WU-Minn-Ox HCP data using the proposed geometric method (Fig. 4a). For all three datasets, the sampling density correction factors for the q(b)=0 sample (a single sample for the averaged b=0 images) are relatively high, which scales up the non-DW signal and translates into an appropriate constant term in the EAP.

The correction factors for non-zero b-values are monotonically increasing, indicating that the signals from high q(b)-values are insufficiently sampled compared to low q(b)-values. The ratios between the correction factors of the lowest and the highest non-zero q-values are: 2.17, 2.89 and 1.76 for the Stanford, MGH-USC HCP and WU-Minn-Ox HCP data

respectively. This means that the sampling density correction operation only moderately scales the signals from high q(b)-values while does not over-emphasize the noise in the low SNR measurements at high q(b)-values. For the MGH-USC HCP data, the slope of the correction factors for non-zero b-values decreases as the b-value increases (Fig. 1b red curve). This is because the MGH-USC HCP protocol partially compensated for the decreased sampling density at high b-values by doubling the number of samples as b-value increases from 3,000 s/mm^2 to 5,000 s/mm^2, as well from 5,000 s/mm^2 to 10,000 s/mm^2.

Figure 5 demonstrates the effects of q-space sampling density correction on the EAP. For the crossing-fiber voxels (from CSO region, Fig. 10 magenta dashed boxes), the 2D coronal cross sections through the center of the 3D EAP (Fig. 5a, b, d, e, g, h), the 1D profiles along left-right (Fig. 5c, f, i red curves), superior-inferior (Fig. 5c, f, i blue curves) and anterior-posterior (Fig. 5c, f, i green curves) directions from the EAP center, and the 3D contours (Fig. 5j, negative values clipped to 0) at different displacement distances are displayed. The EAP becomes sharper after the sampling density correction (comparing Fig. 5j rows i, iii, v with rows ii, iv and vi at displacement distance longer than 0.2 of the MDD_{water}) because the correction scales up high q(b)-value signals. The Gibbs ringing present in the EAP, however, becomes more severe (Fig. 5 pink arrows and dashed circles). The increased intensity of the Gibbs ringing after sampling density correction has the benefit of making the ringing easier to identify (comparing Fig. 5f solid and dashed lines), which assists operations to mitigate the effects of ringing, such as clipping the EAP values beyond the first zero-crossing to 0 before computing metrics and ODF from the EAP. Without sampling density correction, the ringing is harder to identify (e.g. Fig. 5f solid lines) and obscures the shape of EAP (e.g. Fig. 5j, rows iii, displacement distance larger than $0.4 \times MDD_{water}$).

Due to the different q_{max} values for the Stanford, MGH-USC HCP and WU-Minn-Ox HCP datasets, the extents of the recovered EAP are different, i.e. about 2/3 (Fig. 5a, b), 1/2 (Fig. 5d, e) and 1 of MDD_{water} (Fig. 5g, h) respectively. Therefore, the displacement distance at which the 3D EAP contour is the sharpest is different, i.e. $0.6 \times MDD_{water} = 14.2$ um, $0.5 \times MDD_{water} = 8.1$ um, and $1 \times MDD_{water} = 24.4$ um, for the Stanford (Fig. 5j, row ii), MGH-USC HCP (Fig. 5j, row iv) and WU-Minn-Ox HCP data (Fig. 5j, row vi).

Additional EAPs from brain regions where the tissue microstructure is more complex compared to the WM were recovered with q-space sampling density correction. These EAPs were reconstructed in the polar coordinates. For the MGH-USC HCP data, EAPs at 8 μm in ROIs that contain parts of pre- and post-central gyrus, thalamus and brainstem are displayed in Figure 6 (EAPs at 0-10 μm with 0.2 μm step are shown in supplementary videos). These EAPs present the diffusion patterns and map the complicated microstructure without imposing any model on the signal. In the post-central gyrus, for example, the water molecules have a high probability to diffuse in the direction radial to the cortical surface. Interestingly, a portion of the water molecules also tend to diffuse in the direction parallel to the cortical surface, resulting in crossing EAP orientations (Fig. 6b magenta dashed boxes). The sharp EAP contours also reveal multiple directional vectors of water diffusion in different thalamic nuclei and within the basis pontis in the brainstem.

Figures 7 and 8 demonstrate two examples of metrics, i.e. P_r (Fig. 7) and r_α (Fig. 8) that can be derived from the recovered EAP. P_r represents the mean probability of a water molecule within a voxel displacing to a specific distance within the diffusion time used in the pulse sequence. The mean P_r curve averaged from all WM voxels (Fig. 7f red, blue) is narrower than the mean P_r curves for the GM (Fig. 7f green) and cerebrospinal fluid (CSF) in the ventricle (Fig. 7f blue) due to the more constrained water diffusion within the tightly packed axon bundles. At different displacement distances, P_r provides a new type of image contrast based on the diffusion property of the tissue (Fig. 7 b-e). At zero displacement distance, the P_0 map (Fig. 7b) resembles a T_1-weighted image (Fig. 7h, correlation equal to 0.58). Since the probability of water molecules in the WM and GM displacing to ~5.2 μm is similar (Fig. 7f pink arrow), the contrast between WM and GM is diminished in the $P_{5.2\mu m}$ map (Fig. 7c). For a displacement distance slightly longer than 5.2 μm, the P_r for the GM becomes larger than the P_r for the WM. Therefore, the GM is much brighter than the WM in the $P_{7\mu m}$ map, creating a strong GM-WM contrast. The CSF is the brightest in the $P_{15\mu m}$ map since only water molecules with very fast diffusion rate can diffuse to such a long distance.

The r_α index measures the displacement distance that the mean probability decays to α of the maximum probability (i.e. P_0), and hence indicates the overall level of restriction within a voxel. As expected, WM appears darker than the GM and CSF in the r_α maps (Fig. 8 a-f), revealing the increased degree of restricted diffusion within WM.

The r_0 index denotes the longest displacement distance that the water molecules can diffuse. Within the CC, r_0 in the direction perpendicular to the DTI V1 is different in different sub-regions (Fig. 8g, h). Specifically, the r_0 is larger in the body of the CC (Fig. 8g green, 5.65±0.09 μm) compared to the anterior (Fig. 8g red, 5.55±0.15 μm) and posterior part of the CC (Fig. 8g blue, 5.4±0.15 μm). This corresponds well to histological studies in the literature that show that larger axon diameters are only found in the body of the CC and not in the genu and splenium of the CC (92).

The effects of q-space sampling density correction on the ODF are demonstrated in Figure 9. The component ODFs from each shell (Fig. 9 columns 1-6) and the combined ODF (Fig. 9 columns 7-8) reconstructed with (Fig. 9, rows ii, iv, vi) and without (Fig. 9, rows i, iii, v) sampling density correction for the Stanford (Fig. 9 rows i, ii), MGH-USC HCP (Fig. 9 rows iii, iv), and WU-Minn-Ox HCP data (Fig. 9 rows v, vi) are shown. The sampling density correction scales up the signals from high q(b)-value signals (weights determined in Fig. 4b) such that the component ODFs from high q(b)-value shell have higher contribution (larger size, the size of the component ODF from b=1000 s/mm^2 were kept the same with and without the correction) to the combined ODF. Therefore, the combined ODF becomes sharper (comparing Fig. 9, rows i, iii, v with rows ii, iv, vi, column 7), with strengthened ringing obscuring the shape of the ODF and/or leading to "bumps" in the ODF (Fig, 9 green arrows) that might cause erroneous orientations to be used in the tractography. Using the indirect approach with ringing removal (clipping EAP values beyond the first zero crossing to 0), the ODF becomes much cleaner as well as sharper (comparing Fig. 9 columns 7 and 8).

Figure 10 displays the ODF and fiber orientations estimated using both model-based and model-free methods in the crossing fiber ROI from the CSO region. The GDSI ODFs are sharper compared to the GQI ODFs because the sampling density correction increases the contribution from the high q(b)-value signals that contain high frequency information in GDSI. Therefore, intra-voxel crossing fibers appear better delineated in GDSI compared to GQI (more blue and green sticks in Fig. 10b, rows 1, 3, 4, column iv than in column iii). For the model-free methods, detection of crossing fibers appears to be strongly dependent on the maximum b-value. Both GQI and GDSI identify more secondary and tertiary fibers in the MGH-USC HCP data with a maximum b-value of 10,000 s/mm^2 compared to the WU-Minn-Ox HCP data with a maximum b-value of 3,000 s/mm^2. The model-based methods overall identify more secondary and tertiary fibers compared to the model-free methods (more blue and green sticks in Fig. 10b, rows 1, 3, 4, columns i and ii, than in columns iii and iv, and supplementary simulation study).

The fiber crossing angles estimated by the model-based (BEDPOSTX and CSD) and model-free (GDSI) methods follow distinct distributions as depicted in Supplementary Figure 1 and Figure 11. The BEDPOSTX, CSD and GDSI method identifies a secondary fiber in 91%, 84% and 59% and a tertiary of fiber in 63%, 47% and 19% of all WM voxels in the MGH-USC HCP data, and identifies a secondary fiber in 95%, 78% and 9% and a tertiary of fiber in 70%, 26% and 0.7% of all WM voxels in the WU-Minn-Ox HCP data. For BEDPOSTX and CSD, the fiber crossing angle histograms show a peak ~60°, with an exception for the crossing angle between the primary and secondary fibers from the MGH-USC data (Fig. 11a, red curve, histogram peak shifted to ~30°). The fiber crossing angle histograms from CSD also have a preference for ~90°. For GDSI, the fiber crossing angle distribution resembles a half Gaussian curve centered at 90°.

Discussion

Here we present a generalized DSI framework to recover the model-free EAP from non-Cartesian diffusion data. Unlike conventional DSI, GDSI does not require Cartesian q-space sampling and FFT-based reconstruction. GDSI computes the EAP by multiplying the sampling non-uniformity corrected q-space samples with a DFT matrix, and is therefore flexible with the coordinate systems of both the q-space signals and the EAP. We demonstrate various metrics, such as the zero displacement probability, mean probability at a specific displacement distance, and the mean displacement distance at a fraction of the maximum probability, can be derived from multi-shell diffusion data using our method to characterize tissue microstructure. Using the GDSI framework, we also elucidate the contribution and combination of q-space signals to the diffusion ODF by formulating the reconstruction as a linear system, and compute the model-free diffusion ODF from the multi-shell diffusion data.

The model-free EAP from GDSI is equivalent to the raw diffusion data, but provides a more intuitive representation in the Fourier domain, which more directly relates to the underlying diffusion patterns. For example, the shape of the EAP can reflect the restriction and non-Gaussianity of the diffusion process, which is useful for differentiating different tissue types (Fig. 7) and abnormal tissues. The size of the EAP (i.e. the width at the first zero-crossing)

measures the longest displacement distance a water molecule can transverse during the diffusion time, which might reflect the trend of axon/nerve diameter (Fig. 8). This information provided by the EAP may be useful for microstructural imaging. Since the EAP also provides the ODF (EAP's angular summarization) for tractography purpose, the EAP potentially enables a way to integrate the microstructural imaging and diffusion tractography for characterizing microstructural properties associated with specific white matter fiber bundles (93-95).

The displacement distance associated with the GDSI EAP is different from the ground truth for two reasons. First, the narrow pulse assumption ($\delta<<$), a condition of the Fourier relationship between the q-space signals and the EAP, cannot be met in practice. Therefore, the EAP describes the displacement of a spin from the mean position during the first pulsed gradient to the mean position during the second pulsed gradient. Consequently, the displacement distance is underestimated (41, 82). Second, truncating the q-space before the signal decays to zero contaminates the EAP by convolving the true EAP with a point spread function (PSF) after the Fourier transform. The main lobe of the PSF blurs the EAP. The displacement distance is therefore overestimated (96). Therefore, any interpretation of displacement distance metrics derived from the EAP, such as r_α, should account for these approximations.

Fortunately, many approaches now exist to reduce the influence of these two issues on the EAP. For example, the stronger gradient strength provided by the HCP scanners (up to 300 mT/m from MGH-USC, and up to 80 mT/m from WU-Minn-Ox) achieves higher maximum b-values with shorter gradient durations, which not only brings the PGSE experiments closer to the narrow pulse approximation but also helps to mitigate the effects of q-space truncation. Alternatively, q-space truncation effects can be mitigated by deconvolving the EAP with the PSF associated with a specific q-space truncation (97) and reducing the noise floor for diffusion signal at high b-values using the real part rather than the magnitude of the signal (98).

Our proposed EAP reconstruction method relies on solving the Fourier transform using a matrix formalism, i.e. multiplying the q-space signals with a DFT matrix. This approach allows performing the Fourier transform on signals acquired with any q-space sampling pattern, such as multi-shell, and provides a more general form of DSI. Therefore, the proposed GDSI method enables a more direct way to compare the DSI based approach with many other model-based methods, such as CSD, on the same multi-shell data, without the confound of the different datasets required for different methods (e.g. Cartesian sampling data for DSI versus multi-shell sampling data for other model-based methods). The crossing fiber detection of model-free methods was found strongly dependent on the maximum b-value and less sensitive compared to the model-based methods (Fig. 10, Fig. 11), which provides a way to determine the choice of model-free or model-based methods for different datasets for tractography in practice. For example, the model-free methods identify very few secondary and tertiary fibers for the WU-Minn-Ox HCP data with a maximum b-value of 3,000 s/mm^2 while identify similar numbers of secondary and tertiary fibers compared to the model-based methods for the MGH-USC HCP data with a maximum b-value of 10,000 s/mm^2. More interestingly, the distributions of the fiber crossing angles identified by the

model-free and model-based methods were found to follow very different distributions in the WM on the same multi-shell data (Fig. 11) (99).

Cartesian q-space samples acquired in DSI could also benefit from GDSI's matrix formalism reconstruction. For example, the diffusion-encoding directions must be rotated to account for subject motion (45) and gradient nonlinearity (61), in which case the resultant q-space samples might no longer locate on a strict Cartesian grid. Errors will be introduced into the EAP if performing an FFT of the shifted samples. The shifted q-space samples could be interpolated back onto a Cartesian grid, but this requires extra computation. Applying GDSI's matrix formalism EAP reconstruction method directly to the shifted samples offers a more accurate and direct computation of the EAP.

DFT matrix reconstruction also allows the flexibility to recover the EAP at an arbitrary set of displacement directions and distances, e.g. on a Cartesian grid or on radial lines along multiple directions. Recovering the EAP on radial lines is useful for visualizing and analyzing the EAP. To the first point, a 3D EAP can be decomposed as a set of spherical functions at different displacement distances, which can be displayed using the diffusion ODF visualization tools (Figure 6 and supplementary videos). To the second point, there is no need to resample the EAP recovered from FFT-based reconstruction onto radial lines (as performed in DSI) to compute the diffusion ODF and many other orientation-specific EAP metrics (Figures 7 and 8). Finally, along each radial line the EAP values beyond the first zero-crossing can be clipped to 0 to mitigate the Gibbs ringing, which results from the Fourier transform of the truncated q-space. The ringing can otherwise obscure the ODF shape and lead to erroneous fiber orientations (Figs. 3, 4) (83, 96). In DSI, the negative lobes of the ringing present in the EAP are clipped to 0 to mitigate ringing.

A valid DFT matrix reconstruction on non-Cartesian, such as multi-shell, q-space sample requires uniform and sufficient q-space sampling density. However, the q-space sampling density is usually non-uniform. In multi-shell sampling, it is common to slightly under-sample the high q(b)-value regions (Fig. 4b). A sampling density correction is therefore needed to scale up the high q(b)-value signals, which contain high frequency information of the diffusion pattern. Here, we propose a fast geometrical method to estimate the q-space density correction factor that is similar to that used for image reconstruction of radial k-space samples (91). This method makes an assumption that the q-space points are uniformly distributed on each shell, which is true for most multi-shell diffusion data, because of the requirement for uniform angular resolution. Advanced numerical methods such as using a 3D Voronoi diagram (90) can be adopted for other q-space sampling patterns. The sampling density requirements for the multi-shell q-space sampling can be prescribed between shells (Appendix B Eq. B2) and within individual shell (Appendix B Eq. B6). These requirements have to be satisfied to avoid aliasing artifacts in the diffusion propagator reconstructed using GDSI (96, 100). For the multi-shell data used in this study, including those from the HCP, the sampling density requirements are satisfied. For undersampled multi-shell data, a model-based approach or q-space compressed sensing techniques (101, 102) should be adopted.

In GDSI's matrix formalism, the mapping from the q-space signals to the diffusion ODF can be formulated as a linear system, which provides intuition on the diffusion ODF

reconstruction. Specifically, the diffusion ODF value along a specific direction is a linear weighted summation of all the q-space samples, with the linear weights determined by the q-space location of the samples (Eq. 9 and Fig. 1). In the special case of the single-shell sampling, GDSI is consistent with QBI's use of the Funk-Radon transform that approximates the diffusion ODF value along a specific direction as the summation of the q-space signals along the orthogonal equator (Fig. 1e). Further, GDSI is equivalent to GQI in terms of ODF reconstruction if GQI's input signals are precompensated to account for q-space sampling non-uniformity. The difference of the two methods is that GQI solves the ODF analytically while GDSI solves the ODF using a matrix formalism. Compared to GQI, GDSI has the additional freedom to modify the EAP before ODF calculation (e.g. clipping the negative lobes of the ringing to 0 to mitigate ringing), and select the starting point (0 in GQI) (83) and the power of displacement distance (0 and 2 in GQI) in the EAP integration for calculating the ODF, in addition to the benefit of recovering the EAP. GDSI unifies DSI, QBI and GQI in theory and can be used as a replacement in practice. GDSI's linear system formalism also allows decomposition of a diffusion ODF into a series of component ODFs from each q-space sampling point, or each q-space shell (Eq. 10, Figs. 3 and 9). This decomposition is potentially useful for protocol optimization.

In terms of computation, the matrix based reconstruction requires N/log(M) (N is the number of q-space signals, M is the number of EAP values) more multiplications and additions compared to the FFT-based reconstruction, but saves the computations of gridding multi-shell samples to the Cartesian grid and/or interpolating the EAP recovered on the Cartesian grid to radial lines to compute the ODF. N is relatively small for the q-space signals ($\sim10^2$), in contrast to the number of k-space signals in a zero-padded 2D matrix ($\sim10^4$). Further, the simple computation of multiplication and addition in the matrix based reconstruction can be easily accelerated via parallel computing and the use of graphics processing units.

Summary

This study presents a generalized DSI framework named GDSI to recover the model-free spin displacement EAP from multi-shell diffusion MRI data. The proposed GDSI method involves correcting for the non-uniform q-space sampling density and performing the Fourier transform using a DFT matrix. GDSI is shown to produce the EAP and ODF that are in good agreement with those reconstructed from a full DSI acquisition, and to be broadly applicable to different types of multi-shell data including those from the HCP. The maps of EAP metrics such as P_r and r_a are demonstrated as additional means to characterize the diffusion patterns in different tissue types. GDSI also enables fiber orientations estimated from both the model-free and model-based methods on the same multi-shell data. Lastly, GDSI elucidates the contribution and combination of q-space samples to the diffusion ODF and relationship between various diffusion ODF reconstruction methods. In conclusion, our study provides a generalized DSI framework for recovering the EAP and ODF from Cartesian and multi-shell diffusion data, which contributes to the theoretical understanding of the DSI methodology, and flexibility of diffusion MRI data analysis for studying microstructure and connectivity in the human brain.

Supplementary Material

Refer to Web version on PubMed Central for supplementary material.

Acknowledgments

Appendix A

The dephasing term Φ of a spin is proportional to the scalar product between the applied gradient wave vector $\boldsymbol{q}$ ($=q\boldsymbol{v}$) and the relative spin displacement $\boldsymbol{r}$ ($=r\boldsymbol{u}$) as:

$$\Phi = 2\pi \boldsymbol{q}\boldsymbol{r} = 2\pi \cdot q\boldsymbol{v} \cdot r\boldsymbol{u} \quad \text{(A1)}$$

, where unit vectors $\boldsymbol{v}$ and $\boldsymbol{u}$ are directions of $\boldsymbol{q}$ and $\boldsymbol{r}$.

q can be expressed in terms of b for pulsed gradient waveform as:

$$q = \frac{1}{2\pi}\gamma g\delta = \frac{1}{2\pi}\sqrt{\frac{b}{\Delta - \frac{\delta}{3}}} \quad \text{(A2)}$$

, where   is the diffusion time, the interval between the two diffusion encoding gradient pulses during which spins are allowed to displace, and δ is the diffusion-encoding gradient strength. γ is the gyromagnetic ratio ($\gamma/2\pi$=42.58 MHz/T). g is the diffusion-encoding gradient strength.

Any arbitrary displacement distance r can be expressed as a ratio λ of the mean displacement distance of free water (MDD_{water}) at 37°C as:

$$r = \lambda \cdot MDD_{water}. \quad \text{(A3)}$$

For a specific diffusion pulse sequence with given   and δ, MDD_{water} is a constant number, which can be calculated using Einstein's equation (1):

$$MDD = \sqrt{6D(\Delta - \frac{\delta}{3})} \quad \text{(A4)}$$

, where D is the diffusion rate and $-\delta/3$ is the effective diffusion time. MDD_{water} is equal to $\sqrt{6D_{water}(\Delta - \frac{\delta}{3})}$, with the diffusion rate of free water at 37°C D_{water}=2.5×10^{-3} mm^2/s.

Substituting Equations A2, A3 and A4 into Equation A1 provides an expression for Φ in terms of the b-value, the b-vector and a ratio to the MDD_{water}:

$$\Phi = 2\pi \cdot \frac{1}{2\pi}\sqrt{\frac{b}{\Delta - \frac{\delta}{3}}}\boldsymbol{v} \cdot \lambda\sqrt{6D_{water}(\Delta - \frac{\delta}{3})}\boldsymbol{u} = \sqrt{6D_{water}b}\boldsymbol{v} \cdot \lambda\boldsymbol{u}. \quad \text{(A5)}$$

Since the b-value (b) and the b-vector ($\boldsymbol{v}$) are commonly reported in most diffusion pulse sequences, it is more convenient to use Equation A5 rather than Equation A1.

Appendix B

The field of view determined by the q-space sampling density $\triangle q$ should be larger than the extent of the ensemble average propagator (EAP) to avoid aliasing, as:

$$\frac{1}{\triangle q} \geq 2 \cdot MDD \quad \text{(B1)}$$

, where $2 \cdot MDD$ (mean displacement distance given in Eq. A4) is used to approximate the size of the EAP (96). The MDD of free water (MDD_{water}) can be used to provide an upper bound of the EAP size.

For the multi-shell q-space sampling, the sampling density should be sufficient between shells as well as within individual shell. For two arbitrary neighboring shells with b-values of b_1 and b_2 ($b_2 > b_1$), substituting Equations A2 and A4 into Equation B1 gives:

$$\sqrt{b_2 D} - \sqrt{b_1 D} \leq \frac{\pi}{\sqrt{6}} \quad \text{(B2)}$$

, where D is the diffusion coefficient. For an approximate higher bound of the apparent diffusion coefficient in the in vivo human brain of $D=1.7\times10^{-3}$ mm^2/s (the apparent diffusion coefficient along the primary fiber orientation in the corpus callosum measured by DTI (49, 96), the b-value requirement specified in Equation B2 is simplified as:

$$\sqrt{b_2} - \sqrt{b_1} \leq 31 \quad \text{(B3)}$$

, where the unit of b_1 and b_2 is s/mm^2.

On a specific shell with q-value q (b-value b) and N uniformly distributed samples, each sample has a solid angle of $A=4\pi/N$. The solid angle of a sample is also geometrically (Figure Appendix B) determined as:

$$A = 2\pi(1 - \cos\theta). \quad \text{(B4)}$$

The distance between any two samples (ac=bd in Figure Appendix B) on the shell is given by:

$$\Delta q = 2 \cdot q sin\theta. \quad (B5)$$

Substituting Equations A2, A4, B4 and B5 into Equation B1 gives:

$$bD \leq \frac{\pi^2}{96(\frac{1}{N} - \frac{1}{N^2})}. \quad (B6)$$

For D=1.7 × 10^{-3} mm^2/s and assuming $\frac{1}{N^2}$ is negligible (since $\frac{1}{N} \gg \frac{1}{N^2}$), the number of samples N on a shell should satisfy:

$$N \geq \frac{b}{60} \quad (B7)$$

, where b-value has a unit of s/mm^2.

The diffusion coefficient D in Equations B2 and B6 should adapt to different applications accordingly. For example, the apparent diffusion coefficient is as high as ~2.5 χ 10^{-3} mm^2/s for some types of tumor (103) while about 10× lower in the ex vivo brain tissue compared to in the in vivo brain (96).
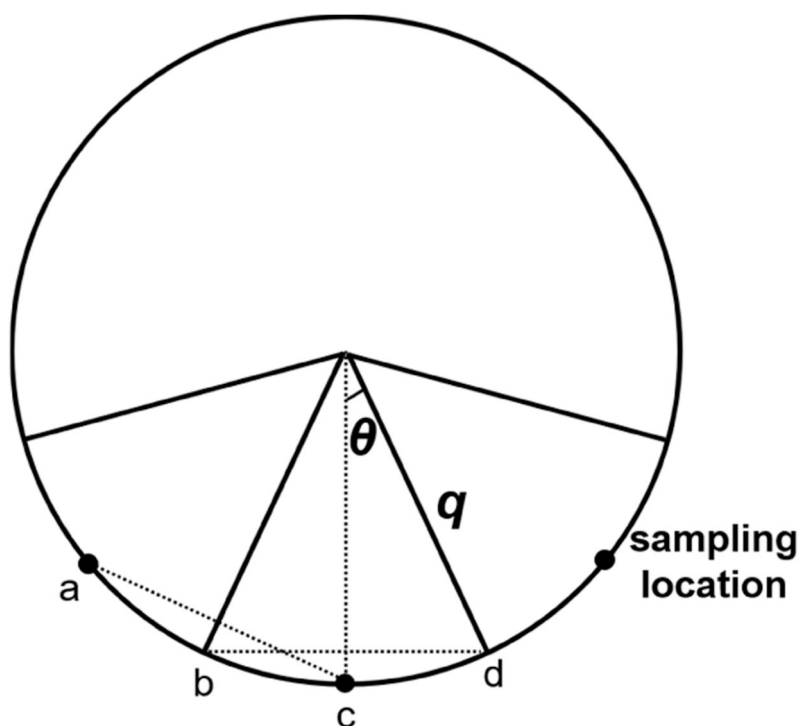
Figure Appendix B.

2D illustration of a q-space sampling shell of q-value q. Radial lines ob and od define the cone associated with the q-space sample c. The distance between two samples (ac) is equal to the distance bd (=$2 \cdot qsin\theta$).

References

1. Einstein A Über die von der molekularkinetischen Theorie der Wärme geforderte Bewegung von in ruhenden Flilssigkeiten suspendierten Teilchen. Annalen der physik. 1905;322(8):549–60.

2. Stejskal E, Tanner J. Spin diffusion measurements: spin echoes in the presence of a time - dependent field gradient. The journal of chemical physics. 1965;42(l):288–92.

3. Stejskal E Use of spin echoes in a pulsed magnetic - field gradient to study anisotropic, restricted diffusion and flow. The Journal of Chemical Physics. 1965;43(10):3597–603.

4. Kärger J, Eleink W. The propagator representation of molecular transport in microporous crystallites. Journal of Magnetic Resonance (1969). 1983 ;51 (1): 1–7.

5. Cory D Measurement of translational displacement probabilities by NMR: an indicator of compartmentation. Magnetic resonance in medicine. 1990; 14(3):435–44. [PubMed: 2355827]

6. Jenner C, Xia Y, Eccles C, Callaghan P. Circulation of water within wheat grain revealed by nuclear magnetic resonance micro-imaging. Nature. 1988;336:399–402.

7. Callaghan PT, Eccles CD, Xia Y. NMR microscopy of dynamic displacements - k-space and q-space imaging. JPhys E Sci Instrum. 1988;21(8):820–2.

8. Twieg DB. The k - trajectory formulation of the NMR imaging process with applications in analysis and synthesis of imaging methods. Medical physics. 1983; 10(5):610–21. [PubMed: 6646065]

9. Ljunggren S A simple graphical representation of Fourier-based imaging methods. Journal of Magnetic Resonance (1969). 1983;54(2):338–43.

10. King MD, Flouseman J, Roussel SA, Van Bruggen N, Williams SR, Gadian DG. q - Space imaging of the brain. Magnetic resonance in medicine. 1994;32(6):707–13. [PubMed: 7869892]

11. King MD, Flouseman J, Gadian D, Connelly A. Localized q - space imaging of the mouse brain. Magnetic resonance in medicine. 1997;38(6):930–7. [PubMed: 9402194]

12. Cohen Y, Assaf Y. High b - value q - space analyzed diffusion - weighted MRS and MRI in neuronal tissues - a technical review. NMR in Biomedicine. 2002;15(7 - 8):516–42. [PubMed: 12489099]

13. Assaf Y, Cohen Y. Structural information in neuronal tissue as revealed by q-space diffusion NMR spectroscopy of metabolites in bovine optic nerve. NMR in Biomedicine. 1999;12(6):335–44. [PubMed: 10516615]

14. Assaf Y, Cohen Y. Assignment of the water slow - diffusing component in the central nervous system using q - space diffusion MRS: Implications for fiber tract imaging. Magnetic resonance in medicine. 2000;43(2):191–9. [PubMed: 10680682]

15. Assaf Y, Mayk A, Cohen Y. Displacement imaging of spinal cord using q-space diffusion-weighted MRI. Magnetic Resonance in Medicine. 2000;44(5):713–22. [PubMed: 11064406]

16. Assaf Y, Ben-Bashat D, Chapman J, Peled S, Biton IE, Kafri M, et al. High b-value q-space analyzed diffusion-weighted MRI: application to multiple sclerosis. Magnetic resonance in medicine : official journal of the Society of Magnetic Resonance in Medicine / Society of Magnetic Resonance in Medicine. 2002;47(1): 115–26.

17. Assaf Y, Chapman J, Ben-Bashat D, Hendler T, Segev Y, Korczyn AD, et al. White matter changes in multiple sclerosis: correlation of q-space diffusion MRI and 1 FI MRS. Magnetic resonance imaging. 2005;23(6):703–10. [PubMed: 16198825]

18. Wedeen V, Reese T, Tuch D, Weigel M, Dou J, Weiskoff R, et al., editors. Mapping fiber orientation spectra in cerebral white matter with Fourier-transform diffusion MRI. Proceedings of the 8th Annual Meeting of ISMRM, Denver; 2000.

19. Wiegell MR, Reese T, Tuch D, Sorensen A, Wedeen V, editors. Diffusion spectrum imaging of fiber white matter degeneration Proc Int Soc Mag Reson Med; 2001.

20. Lin C-P, Wedeen VJ, Chen J-H, Yao C, Tseng W-YI. Validation of diffusion spectrum magnetic resonance imaging with manganese-enhanced rat optic tracts and ex vivo phantoms. NeuroImage. 2003;19(3):482–95. [PubMed: 12880782]

21. Conturo TE, Lori NF, Cull TS, Akbudak E, Snyder AZ, Shimony JS, et al. Tracking neuronal fiber pathways in the living human brain. Proceedings of the National Academy of Sciences. 1999;96(18): 10422–7.

22. Mori S, Crain BJ, Chacko V, Van Zijl P. Three - dimensional tracking of axonal projections in the brain by magnetic resonance imaging. Annals of neurology. 1999;45(2):265–9. [PubMed: 9989633]

23. Wedeen VJ, Rosene DL, Wang R, Dai G, Mortazavi F, Hagmann P, et al. The geometric structure of the brain fiber pathways. Science. 2012;335(6076):1628–34. [PubMed: 22461612]

24. Fujiyoshi K, Hikishima K, Nakahara J, Tsuji O, Hata J, Konomi T, et al. Application of q-space diffusion MRI for the visualization of white matter. The Journal of Neuroscience. 2016;36(9): 2796–808. [PubMed: 26937016]

25. Farrell JA, Zhang J, Jones MV, DeBoy CA, Hoffman PN, Landman BA, et al. q - space and conventional diffusion imaging of axon and myelin damage in the rat spinal cord after axotomy. Magnetic resonance in medicine. 2010;63(5): 1323–35. [PubMed: 20432303]

26. Fatima Z, Motosugi U, Hori M, Onodera T, Ishigame K, Yagi K, et al. Age-related white matter changes in high b-value q-space diffusion-weighted imaging. Neuroradiology. 2013;55(3):253–9. [PubMed: 23053002]

27. Hori M, Yoshida M, Yokoyama K, Kamagata K, Kumagai F, Fukunaga I, et al. Multiple sclerosis: benefits of q-space imaging in evaluation of normal-appearing and periplaque white matter. Magnetic resonance imaging. 2014;32(6):625–9. [PubMed: 24726649]

28. Tanikawa M, Nakahara J, Hata J, Suzuki S, Fujiyoshi K, Fujiwara H, et al. q-Space Myelin Map imaging for longitudinal analysis of demyelination and remyelination in multiple sclerosis patients treated with fingolimod: A preliminary study. Journal of the neurological sciences. 2017;373:352–7. [PubMed: 28088313]

29. Ong HH, Wehrli FW. Quantifying axon diameter and intra-cellular volume fraction in excised mouse spinal cord with q-space imaging. NeuroImage. 2010;51(4): 1360–6. [PubMed: 20350604]

30. Ong HH, Wright AC, Wehrli SL, Souza A, Schwartz ED, Hwang SN, et al. Indirect measurement of regional axon diameter in excised mouse spinal cord with q-space imaging: simulation and experimental studies. NeuroImage. 2008;40(4): 1619–32. [PubMed: 18342541]

31. Hori M, Kamiya K, Nakanishi A, Fukunaga I, Miyajima M, Nakajima M, et al. Prospective estimation of mean axon diameter and extra-axonal space of the posterior limb of the internal capsule in patients with idiopathic normal pressure hydrocephalus before and after a lumboperitoneal shunt by using q-space diffusion MRI. European radiology. 2016;26(9):2992–8. [PubMed: 26694062]

32. Kamiya K, Hori M, Miyajima M, Nakajima M, Suzuki Y, Kamagata K, et al. Axon diameter and intra-axonal volume fraction of the corticospinal tract in idiopathic normal pressure hydrocephalus measured by q-space imaging. PloS one. 2014;9(8):el03842.

33. Wu Y-C, Field AS, Alexander AL. Computation of diffusion function measures in q-space using magnetic resonance hybrid diffusion imaging. Medical Imaging, IEEE Transactions on. 2008;27(6):858–65.

34. Mitra PP, Latour L, Kleinberg RL, Sotak CH. Pulsed-field-gradient NMR measurements of restricted diffusion and the retum-to-the-origin probability. Journal of Magnetic Resonance, Series A. 1995; 114(1):47–58.

35. Descoteaux M, Deriche R, Le Bihan D, Mangin J-F, Poupon C. Multiple q-shell diffusion propagator imaging. Medical image analysis. 2011; 15(4):603–21. [PubMed: 20685153]

36. Assemlal H-E, Campbell J, Pike B, Siddiqi K, editors. Apparent intravoxel fibre population dispersion (FPD) using spherical harmonics. International Conference on Medical Image Computing and Computer-Assisted Intervention; 2011: Springer.

37. Edlow BL, Haynes RL, Takahashi E, Klein JP, Cummings P, Benner T, et al. Disconnection of the ascending arousal system in traumatic coma. Journal of Neuropathology & Experimental Neurology. 2013 ;72(6): 505–23. [PubMed: 23656993]

38. Edlow BL, Copen WA, Izzy S, Kouwe A, Glenn MB, Greenberg SM, et al. Longitudinal diffusion tensor imaging detects recovery of fractional anisotropy within traumatic axonal injury lesions. Neurocritical care. 2016;24(3):342–52. [PubMed: 26690938]

39. Taylor EN, Ding Y, Zhu S, Cheah E, Alexander P, Lin L, et al. Association between tumor architecture derived from generalized Q-space MRI and survival in glioblastoma. Oncotarget. 2017;5.

40. Yamada I, Hikishima K, Miyasaka N, Tokairin Y, Ito E, Kawano T, et al. Esophageal carcinoma: Evaluation with q - space diffusion - weighted MR imaging ex vivo. Magnetic resonance in medicine. 2015;73(6):2262–73. [PubMed: 24947492]

41. Wedeen VJ, Hagmann P, Tseng WYI, Reese TG, Weisskoff RM. Mapping complex tissue architecture with diffusion spectrum magnetic resonance imaging. Magnetic Resonance in Medicine. 2005;54(6): 1377–86. [PubMed: 16247738]

42. Taylor EN, Hoffman MP, Aninwene GE, Gilbert RJ. Patterns of intersecting fiber arrays revealed in whole muscle with generalized Q-space imaging. Biophysical journal. 2015; 108(11):2740–9. [PubMed: 26039175]

43. Hoffman MP, Taylor EN, Aninwene GE, Sadayappan S, Gilbert RJ. Assessing the multiscale architecture of muscular tissue with Q - space magnetic resonance imaging. Microscopy research and technique. 2016.

44. Callaghan PT. Translational dynamics and magnetic resonance: principles of pulsed gradient spin echo NMR: Oxford University Press; 2011.

45. Leemans A, Jones DK. The B - matrix must be rotated when correcting for subject motion in DTI data. Magnetic Resonance in Medicine. 2009;61(6): 1336–49. [PubMed: 19319973]

46. Mesri HY, David S, Viergever M, Leemans A, editors. Investigating the effect of gradient nonlinearities on Diffusional Kurtosis Imaging parameters: Results from the Human Connectome Project. In Proceedings of the 26th Annual Meeting of the International Society for Magnetic Resonance in Medicine (ISMRM), Paris, France; 2018.

47. Guo F, Parker G, De Luca A, Jones D, Viergever M, Leemans A, et al., editors. The influence of gradient nonlinearity on spherical deconvolution approaches: to correct or not to correct? In

Proceedings of the 26th Annual Meeting of the International Society for Magnetic Resonance in Medicine (ISMRM), Paris, France; 2018.

48. Basser PJ, Mattiello J, LeBihan D. MR diffusion tensor spectroscopy and imaging. Biophysical journal. 1994;66(l):259–67. [PubMed: 8130344]

49. Pierpaoli C, Jezzard P, Basser PJ, Barnett A, Di Chiro G. Diffusion tensor MR imaging of the human brain. Radiology. 1996;201 (3):637–48. [PubMed: 8939209]

50. Zhang H, Schneider T, Wheeler-Kingshott CA, Alexander DC. NODDI: practical in vivo neurite orientation dispersion and density imaging of the human brain. NeuroImage. 2012;61 (4): 1000–16. [PubMed: 22484410]

51. Tournier JD, Calamante F, Connelly A. Robust determination of the fibre orientation distribution in diffusion MRI: Non-negativity constrained super-resolved spherical deconvolution. NeuroImage. 2007;35(4): 1459–72. [PubMed: 17379540]

52. Tournier JD, Calamante F, Gadian DG, Connelly A. Direct estimation of the fiber orientation density function from diffusion-weighted MRI data using spherical deconvolution. NeuroImage. 2004;23(3): 1176–85. [PubMed: 15528117]

53. Jeurissen B, Tournier J-D, Dhollander T, Connelly A, Sijbers J. Multi-tissue constrained spherical deconvolution for improved analysis of multi-shell diffusion MRI data. NeuroImage. 2014; 103:411–26. [PubMed: 25109526]

54. Andersson JL, Sotiropoulos SN. An integrated approach to correction for off-resonance effects and subject movement in diffusion MR imaging. NeuroImage. 2016;125:1063–78. [PubMed: 26481672]

55. Jenkinson M, Beckmann CF, Behrens TEJ, Woolrich MW, Smith SM. FSL. NeuroImage. 2012;62(2):782–90. [PubMed: 21979382]

56. Smith SM, Jenkinson M, Woolrich MW, Beckmann CF, Behrens TE, Johansen-Berg H, et al. Advances in functional and structural MR image analysis and implementation as FSL. NeuroImage. 2004;23:S208–S19. [PubMed: 15501092]

57. Vaillancourt O, Chamberland M, Houde J-C, Descoteaux M. Visualization of Diffusion Propagator and Multiple Parameter Diffusion Signal Visualization and Processing of Higher Order Descriptors for Multi-Valued Data: Springer; 2015 p. 191–212.

58. Setsompop K, Kimmlingen R, Eberlein E, Witzel T, Cohen-Adad J, McNab JA, et al. Pushing the limits of in vivo diffusion MRI for the Human Connectome Project. NeuroImage. 2013;80:220–33. [PubMed: 23707579]

59. McNab JA, Edlow BL, Witzel T, Huang SY, Bhat H, Heberlein K, et al. The Human Connectome Project and beyond: initial applications of 300 mT/m gradients. NeuroImage. 2013;80:234–45. [PubMed: 23711537]

60. Fan Q, Nummenmaa A, Witzel T, Zanzonico R, Keil B, Cauley S, et al. Investigating the capability to resolve complex white matter structures with high b-value diffusion magnetic resonance imaging on the MGH-USC connectom scanner. Brain connectivity. 2014;4(9):718–26. [PubMed: 25287963]

61. Sotiropoulos SN, Jbabdi S, Xu J, Andersson JL, Moeller S, Auerbach EJ, et al. Advances in diffusion MRI acquisition and processing in the Human Connectome Project. NeuroImage. 2013;80:125–43. [PubMed: 23702418]

62. Ugurbil K, Xu J, Auerbach EJ, Moeller S, Vu AT, Duarte-Carvajalino JM, et al. Pushing spatial and temporal resolution for functional and diffusion MRI in the Human Connectome Project. NeuroImage. 2013;80:80–104. [PubMed: 23702417]

63. Van Essen DC, Smith SM, Barch DM, Behrens TE, Yacoub E, Ugurbil K. The WU-Minn Human Connectome Project: an overview. NeuroImage. 2013;80:62–79. [PubMed: 23684880]

64. Aganj I, Lenglet C, Sapiro G, Yacoub E, Ugurbil K, Harel N. Reconstruction of the orientation distribution function in single - and multiple - shell q - ball imaging within constant solid angle. Magnetic Resonance in Medicine. 2010;64(2):554–66. [PubMed: 20535807]

65. Kamath A, Aganj I, Xu J, Yacoub E, Ugurbil K, Sapiro G, et al., editors. Generalized constant solid angle odf and optimal acquisition protocol for fiber orientation mapping. MICCAI Workshop on Computational Diffusion MRI; 2012.

66. Tuch DS. Q - ball imaging. Magnetic Resonance in Medicine. 2004;52(6): 1358–72. [PubMed: 15562495]

67. Behrens T, Woolrich M, Jenkinson M, Johansen - Berg H, Nunes R, Clare S, et al. Characterization and propagation of uncertainty in diffusion - weighted MR imaging. Magnetic resonance in medicine. 2003;50(5):1077–88. [PubMed: 14587019]

68. Özarslan E, Shepherd TM, Vemuri BC, Blackband SJ, Mareci TH. Resolution of complex tissue microarchitecture using the diffusion orientation transform (DOT). NeuroImage. 2006;31(3): 1086–103. [PubMed: 16546404]

69. Canales-Rodríguez EJ, Lin C-P, Iturria-Medina Y, Yeh C-H, Cho K-H, Melie-García L. Diffusion orientation transform revisited. NeuroImage. 2010;49(2): 1326–39. [PubMed: 19815083]

70. Descoteaux M, Deriche R, Le Bihan D, Mangin J-F, Poupon C, editors. Diffusion propagator imaging: using Laplace's equation and multiple shell acquisitions to reconstruct the diffusion propagator. International Conference on Information Processing in Medical Imaging; 2009: Springer.

71. Eiosseinbor AP, Chung MK, Wu Y-C, Alexander AL. Bessel fourier orientation reconstruction (bfor): An analytical diffusion propagator reconstruction for hybrid diffusion imaging and computation of q-space indices. NeuroImage. 2013;64:650–70. [PubMed: 22963853]

72. Assemlal H-E, Tschumperlé D, Brun L. Efficient and robust computation of PDF features from diffusion MR signal. Medical image analysis. 2009;13(5):715–29. [PubMed: 19665917]

73. Özarslan E, Koay CG, Shepherd TM, Komlosh ME, rfano lu MO, Pierpaoli C, et al. Mean apparent propagator (MAP) MRI: a novel diffusion imaging method for mapping tissue microstructure. NeuroImage. 2013;78:16–32. [PubMed: 23587694]

74. Beatty PJ, Nishimura DG, Pauly JM. Rapid gridding reconstruction with a minimal oversampling ratio. IEEE transactions on medical imaging. 2005;24(6):799–808. [PubMed: 15959939]

75. Wu Y-C, Alexander AL. Fiybrid diffusion imaging. NeuroImage. 2007;36(3):617–29. [PubMed: 17481920]

76. Yeh F-C, Wedeen VJ, Tseng W. Generalized q-sampling imaging. IEEE transactions on medical imaging. 2010;29(9): 1626. [PubMed: 20304721]

77. Tian Q, Yang G, Leuze CW, Rokem A, Edlow BL, McNab JA, editors. A Comprehensive Analytic Solution of Diffusion Orientation Distribution Function. In Proceedings of the 23rd Annual Meeting of the Organization for Fiuman Brain Mapping (OFiBM), Vancouver, British Columbia, Canada; 2017.

78. Baete SH, Yutzy S, Boada FE. Radial q - space sampling for DSI. Magnetic resonance in medicine. 2015.

79. Baete SH, Boada FE. Accelerated radial diffusion spectrum imaging using a multi - echo stimulated echo diffusion sequence. Magnetic Resonance in Medicine. 2017.

80. Callaghan PT. Principles of nuclear magnetic resonance microscopy: Clarendon Press Oxford; 1991.

81. Callaghan P NMR imaging, NMR diffraction and applications of pulsed gradient spin echoes in porous media. Magnetic resonance imaging. 1996; 14(7):701–9. [PubMed: 8970070]

82. Mitra PP, Fialperin BI. Effects of finite gradient-pulse widths in pulsed-field-gradient diffusion measurements. Journal of Magnetic Resonance, Series A. 1995; 113(1):94–101.

83. Paquette M, Gilbert G, Descoteaux M. Optimal DSI reconstruction parameter recommendations: Better ODFs and better connectivity. NeuroImage. 2016;142:1–13. [PubMed: 27480623]

84. Tian Q, Yang G, Leuze CW, Rokem A, Edlow BL, McNab JA, editors. Model-free Fourier Reconstruction of the Diffusion Propagator from Multi-b-shell Diffusion Data. In Proceedings of the 25th Annual Meeting of the International Society for Magnetic Resonance in Medicine (ISMRM), Honolulu, Hawaii, USA; 2017.

85. Fan Q, Witzel T, Nummenmaa A, Van Dijk KR, Van Horn JD, Drews MK, et al. MGH-USC Human Connectome Project datasets with ultra-high b-value diffusion MRI. NeuroImage. 2016; 124:1108–14. [PubMed: 26364861]

86. van der Kouwe AJ, Benner T, Salat DH, Fischl B. Brain morphometry with multiecho MPRAGE. NeuroImage. 2008;40(2):559–69. [PubMed: 18242102]

87. Andersson JL, Skare S, Ashburner J. How to correct susceptibility distortions in spin-echo echo-planar images: application to diffusion tensor imaging. NeuroImage. 2003;20(2):870–88. [PubMed: 14568458]

88. Dale AM, Fischl B, Sereno MI. Cortical surface-based analysis: I. Segmentation and surface reconstruction. NeuroImage. 1999;9(2): 179–94. [PubMed: 9931268]

89. Fischl B, Dale AM. Measuring the thickness of the human cerebral cortex from magnetic resonance images. Proceedings of the National Academy of Sciences. 2000;97(20): 11050–5.

90. Rasche V, Proksa R, Sinkus R, Bornert P, Eggers H. Resampling of data between arbitrary grids using convolution interpolation. IEEE transactions on medical imaging. 1999;18(5):385–92. [PubMed: 10416800]

91. Pauly J Non-cartesian reconstruction. URL: http://webstanfordedu/class/ee369c/. 2005.

92. Aboitiz F, Scheibel AB, Fisher RS, Zaidel E. Fiber composition of the human corpus callosum. Brain research. 1992;598(1): 143–53. [PubMed: 1486477]

93. Fiuber E, Donnelly PM, Rokem A, Yeatman JD. Rapid and widespread white matter plasticity during an intensive reading intervention. Nature communications. 2018;9(1):2260.

94. Yeatman JD, Richie-Halford A, Smith JK, Keshavan A, Rokem A. A browser-based tool for visualization and analysis of diffusion MRI data. Nature communications. 2018;9(1):940.

95. Yeatman JD, Dougherty RF, Myall NJ, Wandell BA, Feldman HM. Tract profiles of white matter properties: automating fiber-tract quantification. PloS one. 2012;7(11):e49790. [PubMed: 23166771]

96. Tian Q, Rokem A, Folkerth RD, Nummenmaa A, Fan Q, Edlow BL, et al. Q - space truncation and sampling in diffusion spectrum imaging. Magnetic resonance in medicine. 2016.

97. Canales-Rodriguez EJ, Iturria-Medina Y, Aleman-Gomez Y, Melie-Garcia L. Deconvolution in diffusion spectrum imaging. NeuroImage. 2010;50(1): 136–49. [PubMed: 19962440]

98. Eichner C, Cauley SF, Cohen-Adad J, MÖller HE, Turner R, Setsompop K, et al. Real diffusion-weighted MRI enabling true signal averaging and increased diffusion contrast. NeuroImage. 2015;122:373–84. [PubMed: 26241680]

99. Catani M, Bodi I, Dell'Acqua F. Comment on "The geometric structure of the brain fiber pathways". Science. 2012;337(6102): 1605.

100. Tefera GB, Zhou Y, Juneja V, Narayana PA. Evaluation of fiber tracking from subsampled q-space data in diffusion spectrum imaging. Magnetic resonance imaging. 2013;31(6):820–6. [PubMed: 23602724]

101. Bilgic B, Setsompop K, Cohen - Adad J, Yendiki A, Wald LL, Adalsteinsson E. Accelerated diffusion spectrum imaging with compressed sensing using adaptive dictionaries. Magnetic Resonance in Medicine. 2012;68(6): 1747–54. [PubMed: 23008145]

102. Paquette M, Merlet S, Gilbert G, Deriche R, Descoteaux M. Comparison of sampling strategies and sparsifying transforms to improve compressed sensing diffusion spectrum imaging. Magnetic Resonance in Medicine. 2015;73(1):401–16. [PubMed: 24478106]

103. Yamasaki F, Kurisu K, Satoh K, Arita K, Sugiyama K, Ohtaki M, et al. Apparent diffusion coefficient of human brain tumors at MR imaging. Radiology. 2005;235(3):985–91. [PubMed: 15833979]
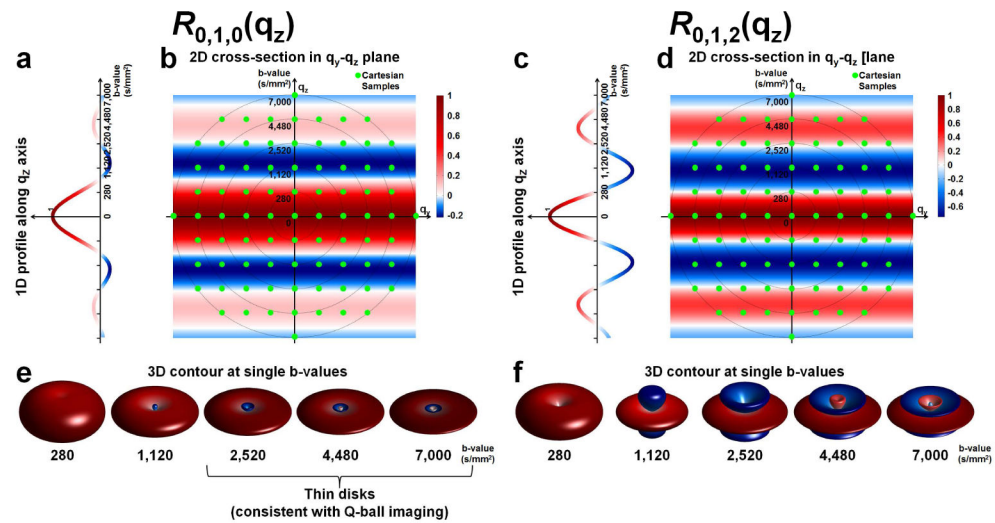
Figure 1.

The reconstruction matrix $R_{0,1,0}(q_z)$ and $R_{0,1,2}(q_z)$ for computing the orientation distribution function value along q_z-axis (bottom to top) with parameters $\lambda_s=0$, $\lambda_e=1$, $n=0$ (a, b, e) and $\lambda_s=0$, $\lambda_e=1$, n=2 (c, d, f). $R_{0,1,0}(q_z)$ and $R_{0,1,2}(q_z)$ are displayed as 1D profile along the q_z-axis (a, c), 2D cross-section on the q_y-q_z plane (b, d), and 3D contour at single q(b)-values (e, f). The green dots display the standard DSI-11 Cartesian q-space sampling locations with 7000 s/mm^2 maximum b-value.
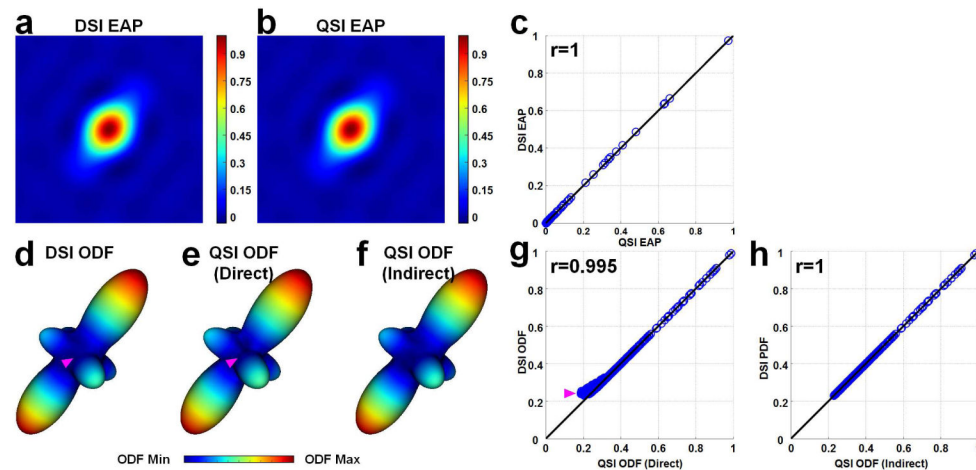
Figure 2.
Comparison of ensemble average propagator (EAP) (a, b) and orientation distribution function (ODF) (d-e) recovered from fast Fourier transform (FFT)-based diffusion spectrum imaging (DSI) (a, d) and proposed matrix formalism-based (q-space imaging) QSI reconstruction (b, e, f) on a simulated noise-free three-fiber-crossing DSI-11 voxel. For both methods, the ODFs are reconstructed with $\lambda_s = 0$, $\lambda_e = 1$, n=2. The ODF from the indirect QSI approach (f) was computed with the negative values of the EAP clipped to 0, the practice used in DSI reconstruction. The EAP and ODF are normalized by their maximum values. The scatter plots (c, g, h) depict 500 randomly selected values, with correlation from all values reported. The pink arrows highlight a region on ODF that demonstrates the effects of clipping negative values in EAP to 0 on the consequently reconstructed ODF.
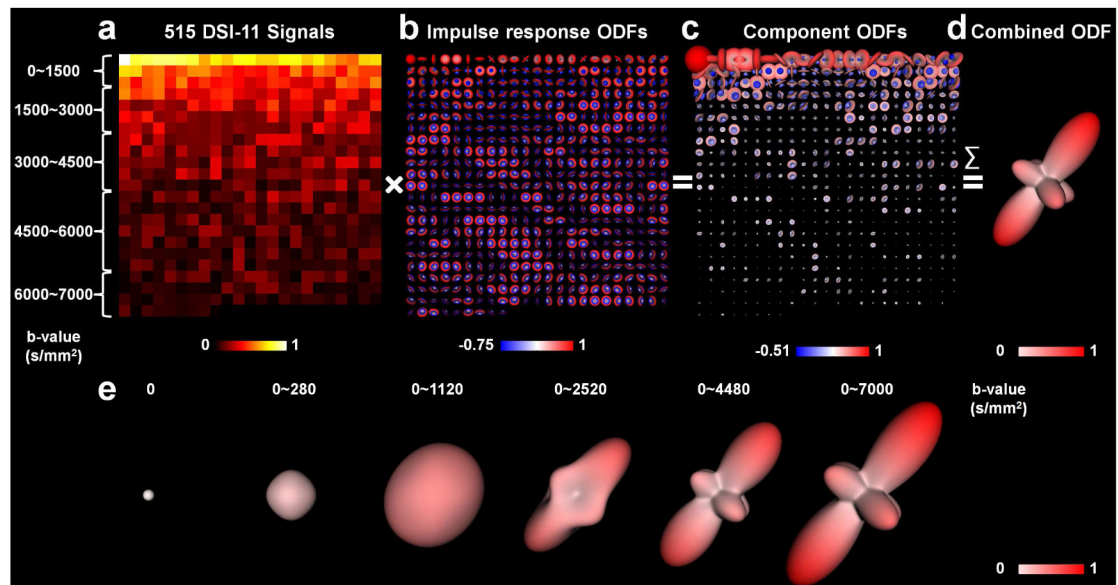
Figure 3.

Decomposition of the orientation distribution function (ODF) from the simulated noise-free three-fiber-crossing voxel (d) acquired using a standard diffusion spectrum imaging acquisition with $11 \times 11 \times 11$ Cartesian grid and 7000 s/mm^2 maximum b-value into component ODFs (c) from the 515 q-space signals (a), and component ODFs (e) from q-space signals with different maximum b-values (the six b-values along the left-right axis, i.e. 0, 280 s/mm^2, 1120 s/mm^2, 2520 s/mm^2, 4480 s/mm^2, 7000 s/mm^2). The q-space signals in (a) are arranged from low to high b-value in a 2D matrix (left to right, top to bottom). Each component ODF in (c) is the impulse response ODF (b) weighted by the diffusion signal intensity measured at the correspondent q-space location. The size of the impulse response ODF (b), component ODF (c, e) is proportional to the ODF value.
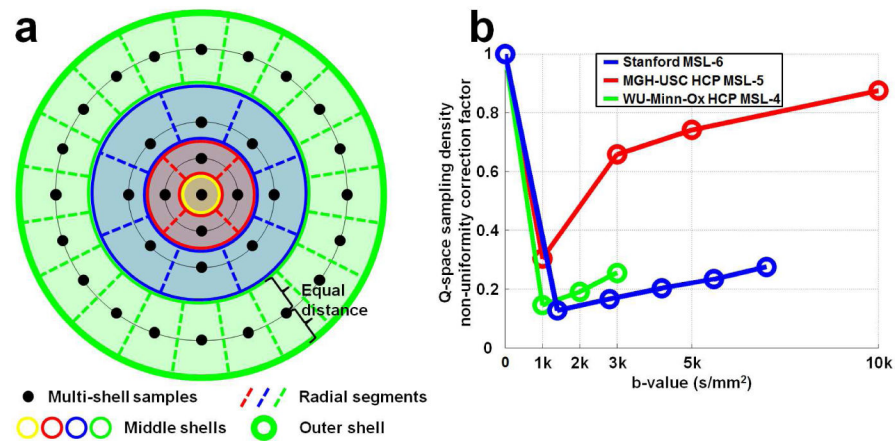
Figure 4.
A 2D illustration of the proposed geometrical approach to estimate the q-space sampling density correction factor, i.e. the volume associated with each q-space sample, assuming q-space samples are uniformly distributed on each shell (a), and the estimated results at each shell for the Stanford (b, blue curve), MGH-USC HCP (b, red curve) and WU-Minn-Ox HCP data (b, green curve). Four shells are depicted (including the origin) for illustration purpose. Note in (b) the x-axis is specified in b-value, which is square of the corresponding q-value.
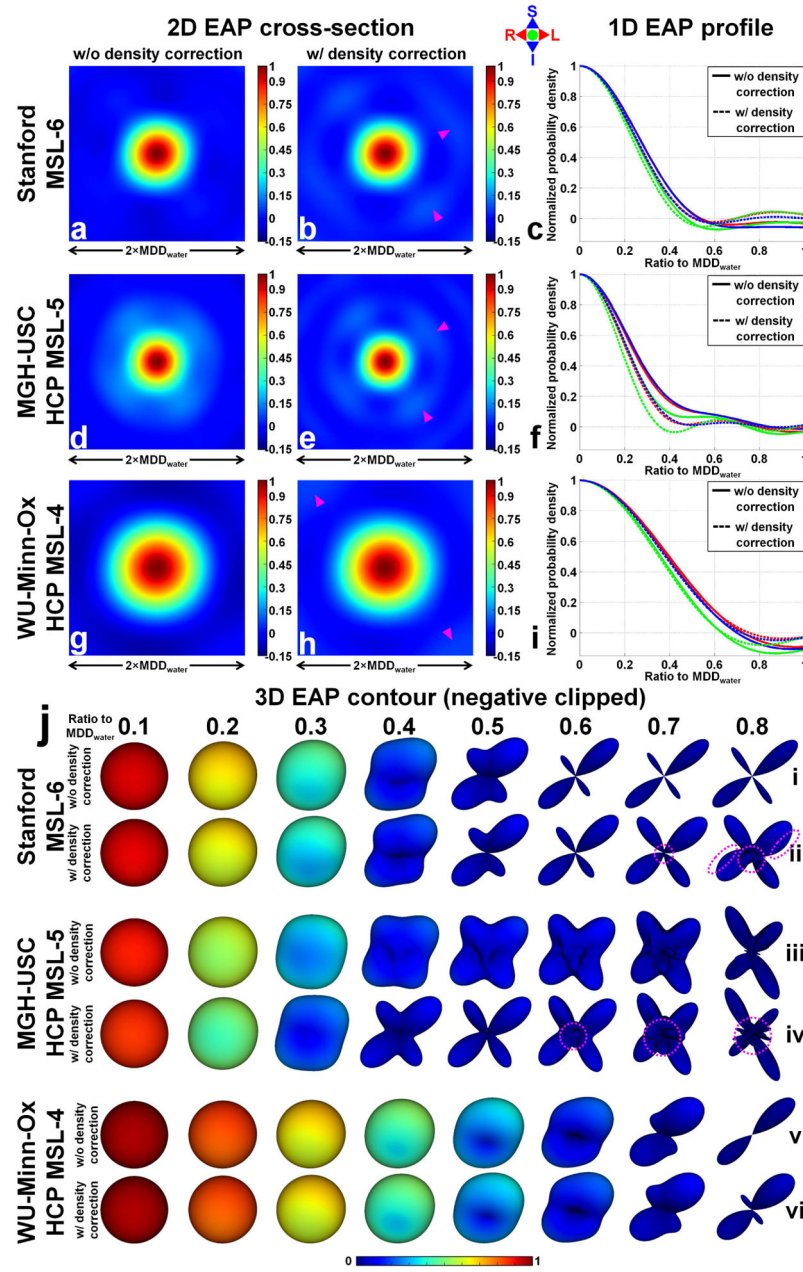
Figure 5.
Reconstructed spin displacement ensemble average propagator (EAP) with (b, e, h, dashed lines in c, f, i, and rows ii, iv, vi in j) and without (a, d, g, solid lines in c, f, i, and rows i, iii, v in j) q-space sampling density correction of crossing-fiber voxels (Fig. 10 green dashed boxes) from the Stanford (a-c, row i and ii in j), MGH-USC HCP (d-f, rows iii and iv in j) and WU-Minn-Ox HCP data (g-i, rows v and vi in j). The 2D coronal cross sections through the center of the 3D EAP (a, b, d, e, g, h), the 1D profiles along left-right (L-R, red lines in c, f, i), superior-inferior (S-I, blue lines in c, f, i) and anterior-posterior (A-P, green lines in c, f, i) directions from the EAP center, and the 3D contours (j, negative values clipped to 0) at different displacement distances are displayed. The mean displacement distance of free

water (MDD_{water}) given the experimental timing is 23.7 μm, 16.2 μm, and 24.4 μm for the Stanford, MGH-USC HCP and WU-Minn-Ox HCP data respectively. The EAPs are normalized by their maximum values (i.e. the value at the EAP center). The pink arrows and dashed circles highlight the positive side lobes of the Gibbs ringing.
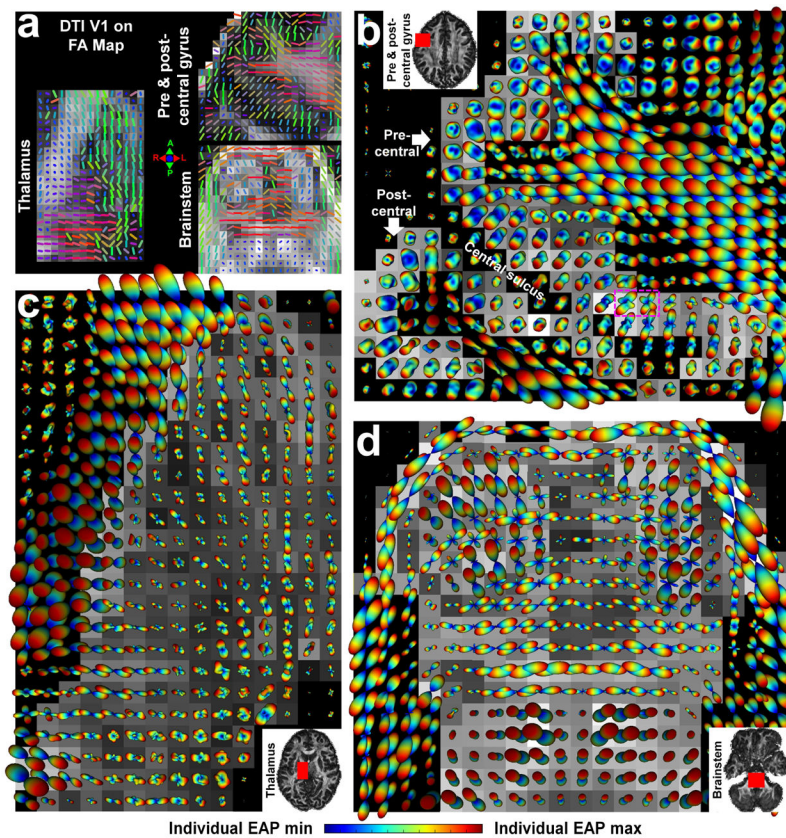
Figure 6.
Spin displacement ensemble average propagators (EAPs) recovered at 8 μm (with q-space sampling density correction) from the pre- and post-central gyrus, thalamus and brainstem regions of interest (ROIs, red rectangles in the inset images in b-d) from the MGH-USC HCP data overlaid on axial slices of fractional anisotropy (FA) maps (windowed between [0, 1]) from diffusion tensor imaging (DTI) (b-d). The nearby voxels outside the gray matter, thalamus and brainstem within the ROIs are on top of black background. The FA and the primary eigenvectors (V1) from DTI of the three ROIs are displayed in (a). DTI V1 is color coded based on orientation (red: left-right, green: anterior-posterior, blue: superior-inferior).
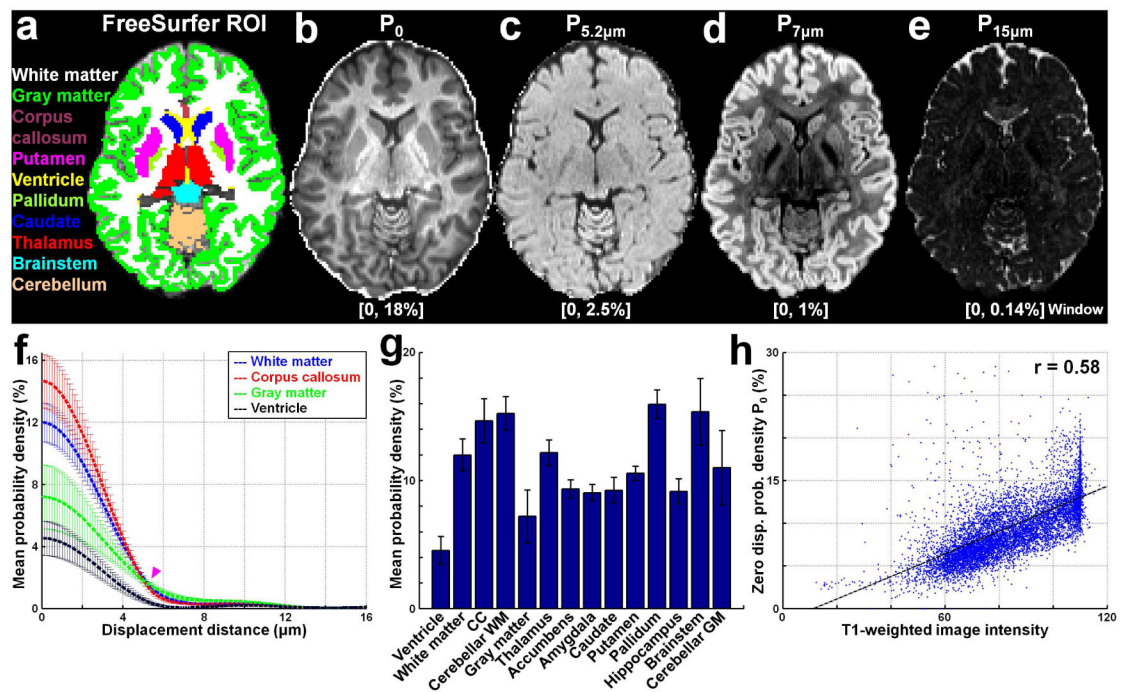
Figure 7.
Maps of the mean probability at 0 (b), 5.2 μm (c), 7 μm (d) and 15 μm (e) displacement distance on a representative axial slice, and the mean and standard deviation of the mean probability (f, g) within 14 FreeSurfer regions of interest (ROIs) (a, listed along the x-axis in g) from the MGH-USC HCP data. The scatter plot of the zero-displacement probability versus the T1-weighted image intensity in the whole brain is showed with the correlation value (h).
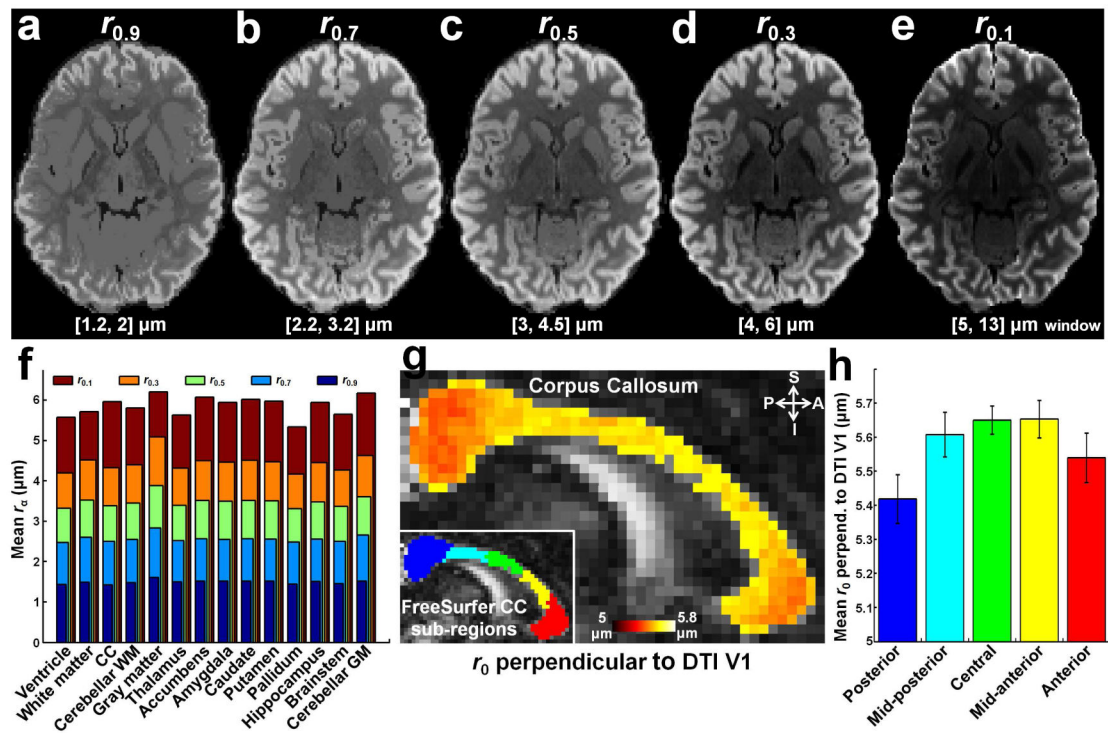
Figure 8.
Maps of the displacement distance at 0.9 (a), 0.7 (b), 0.5 (c), 0.3 (d), and 0.1 (e) of the zero displacement probability (P_0) on a representative axial slice, and their mean within 14 FreeSurfer region of interests (ROIs) (Fig. 7a, listed along the x-axis in f) from the MGH-USC HCP data. The map of the displacement distance at 0 probability (r_0, distance at first zero crossing) perpendicular to the primary eigenvector (V1) from diffusion tensor imaging (DTI) in the corpus callosum (CC) is displayed on fractional anisotropy (FA) map (windowed between [0, 1]) from DTI on a representative sagittal slice. The mean and standard deviation of r_0 within the five sub-regions of the CC (the anterior (red in g inset), mid-anterior (yellow in g inset), central (green in g inset), mid-posterior (cyan in g inset) and posterior (blue in g inset)) are reported in (h). Only voxels with FA larger than 0.5 within the FreeSurfer CC ROI are included.
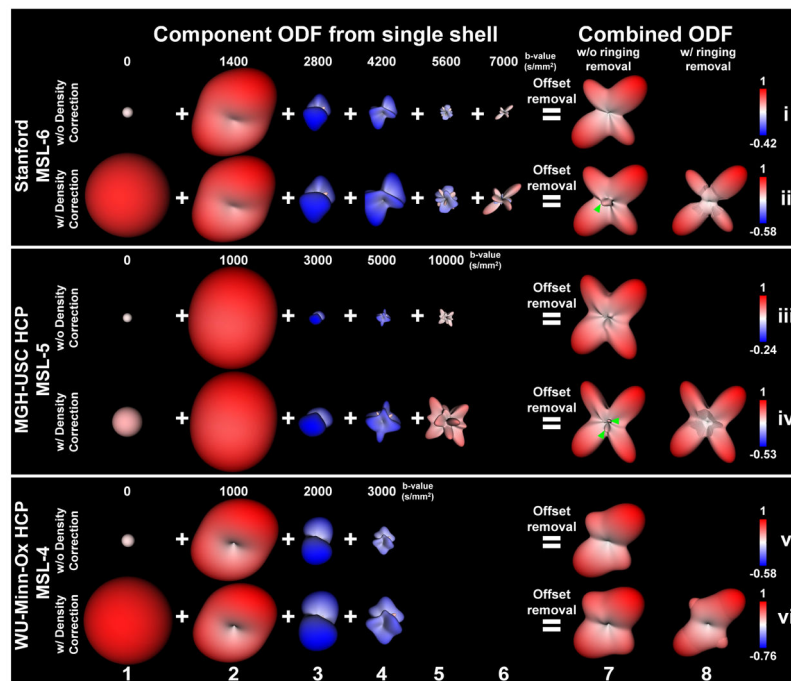
Figure 9.
Component orientation distribution functions (ODFs) from single shell (columns 1-6) and combined ODF (columns 7, 8) reconstructed with (rows ii, iv, vi) and without (rows i, iii, v) q-space sampling density correction, with (column 8) and without (column 7) ensemble average propagator (EAP) ringing removal for the Stanford (rows i, ii), MGH-USC HCP (rows iii, iv) and WU-Minn-Ox HCP data (rows v, vi). The size of the component ODF is proportional to their value. The size of the component ODF from the b=1000 s/mm^2 shell is kept the same with and without q-space sampling density correction. The combined ODF is normalized by their maximum.
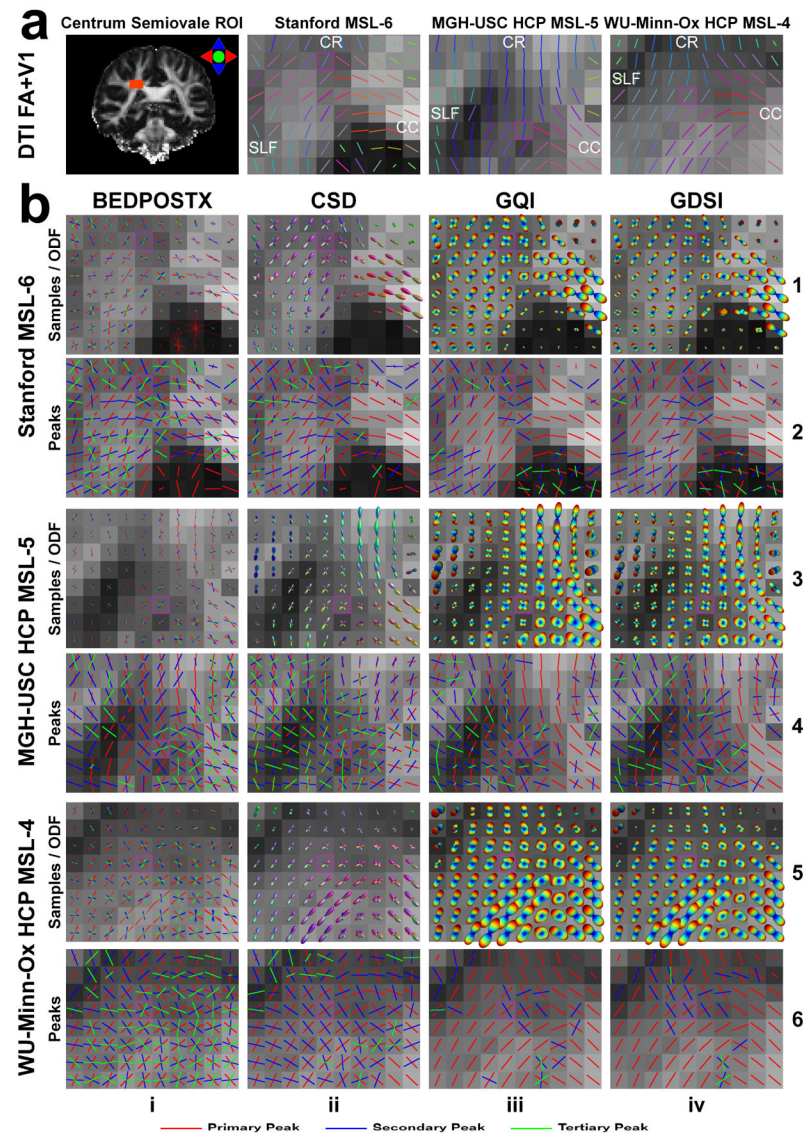
Figure 10.
Reconstructed fiber orientation samples (b, rows 1, 3, 5, columns i, 15 randomly selected samples, stick length proportional to the fiber volume fraction) and the average orientation (b, rows 2, 4, 6, columns i) from the BEDPOSTX method, and the orientation distribution function (ODF) (b, rows 1, 3, 5, columns ii-iv) and the ODF peaks (b, rows 2, 4, 6, columns ii-iv) from the multi-shell multi-tissue constrained spherical deconvolution (CSD) method, generalized q-space imaging (GQI), and the proposed generalized diffusion spectrum imaging (GDSI) method in the centrum semiovale region (a) from the Stanford (b, rows 1, 2), MGH-USC HCP (b, rows 3, 4) and WU-Minn-Ox HCP data (b, rows 5, 6). The primary eigenvectors (V1) from diffusion tensor imaging (DTI) are also depicted (a). All reconstruction results are displayed on top of the DTI fraction anisotropy (FA) map (windowed between 0 and 1). The diffusion ODF (b, rows 1, 3, 4, columns iii and iv) is color coded with the minimum as blue and the maximum as red. The red, blue and green vectors from the ODF peaks and BEDPOSTX (b, rows ii, iv, vi) represent the primary,

secondary and tertiary diffusion orientations, respectively. DTI V1 and the fiber ODF (b, rows 1, 3, 4, columns ii) is color coded based on orientation (red: left-right, green: anterior-posterior, blue: superior-inferior). The centrum semiovale region contains intersection of the corpus callosum (CC), the corona radiata (CR), and the superior longitudinal fasciculus (SLF). The magenta dashed boxes indicate the crossing-fiber voxels presented in Figures 5 and 9.
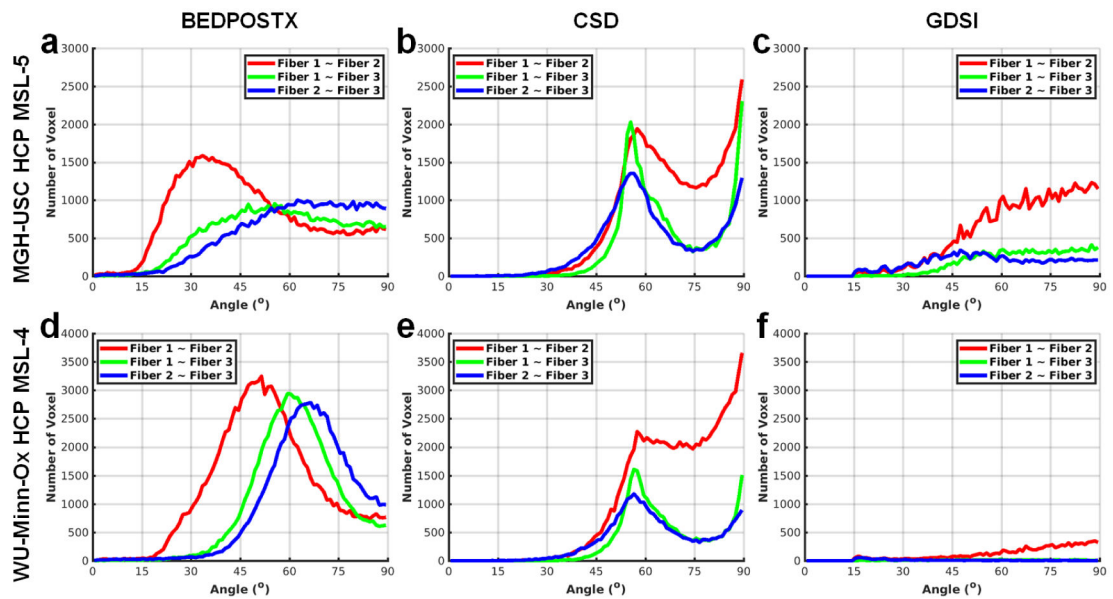
Figure 11.
Histograms of the angles between the primary, secondary and tertiary fiber orientations identified by the BEDPOSTX method (a, d), the multi-shell multi-tissue constrained spherical deconvolution (CSD) method (b, e), and the proposed generalized diffusion spectrum imaging (GDSI) method from the MGH-USC HCP (a-c) and WU-Minn-Ox HCP (d-f) multi-shell data. The histograms only include white matter voxels with both the primary and secondary fibers (red curves), both the primary and tertiary fibers (green curves) and both the secondary tertiary fibers (blue curves). The area under the red, green and blue curves is equal to the nur of the secondary fibers, tertiary fibers and tertiary fibers, respectively.